We thank the reviewers for the input and resulting improvements to the manuscript.

Response to Reviewer 1:

Minor and technical comments:
(1) lines 105-107: '. . . the anthropogenic molecules have a tendency to reduce water uptake and thereby REDUCE the viscosity of the mixed particles.' I believe you meant to say '. . . ENHANCE the viscosity'.

Thank you. The correction is made.

(2) lines 101-103: these statements are also supported by the model calculations of Berkemeier et al. (Atmos. Chem. Phys., 14, 12513–12531, 2014.) suggesting that the anthropogenic aromatic SOA precursors naphthalene may lead to higher-viscosity secondary organic material when compared to biogenic precursors such as pinene and isoprene.

This reference is added.

(3) In Figure 2b the dashed red line indicating 'pollution at night' is missing. Is this by accident or intentional?

For Figure 2b, there were no data that fit the classification of "pollution at night". The figure caption is clarified, as follows: *"No data sets fit the classification of Manaus pollution during the nighttime of IOP2 (i.e., absence of red dashed line in panel (b))."*

(4) lines 368-379 and Figure 7: the hygroscopicity was measured using different approaches. This is openly discussed in the text, but I would like you to mention that _CCN and _HGF can be quite different for solutes that form non-ideal aqueous solutions. Therefore, I suggest to indicate in the Figure (or at least in the figure caption) that the plotted _-values were obtained by different methods at different humidity.

κ_{CCN} and κ_G are now included in Figure 7. The following clarification is added to the figure caption: "*Different techniques were used to measure κ_G and κ_{CCN}, as described in the main text.*"

The main text is changed by deleting two sentences and replacing them with the following: "Sub- and supersatured κ values can be systematically different (Petters and Kreidenweis, 2007; Ruehl et al., 2016)."

Response to Reviewer 2:
1) Page 11, line 226: "Calibration of the impactor shows a transition from rebound to adhesion between 102 to 1 Pa s in viscosity for sucrose particles (Bateman et al., 2015)." To relate particle bounce to viscosity values, more than one substance should be used in calibrations. The particle bounce properties are not affected only by viscosity, but also other material characteristics which may vary between different substances.

We agree with the reviewer that a more robust understanding of material physical properties as related to their rebound behavior would be beneficial for a more complex analysis of ambient particle rebound behavior. The transition from semisolid to liquid for a variety of inorganic compounds with respect to rebound behavior in this same apparatus has recently been studied (Li et al., 2016). In the absence of a complete study on a variety of material characteristics and their rebound response, the present study assumes that the uptake of water by semi-solid sucrose particles to liquid is a valid model system for the transition of SOM from semi-solid to liquid.

The text is expanded as follows: "*As a point of reference, the transition from rebound to adhesion occurs across a viscosity transition of 10^2 to 1 Pa s for sucrose particles for the operating conditions of the impactor (Bateman et al., 2015). The viscosity range corresponding to the rebound transition can depend on particle composition, but this aspect is not investigated herein.*"

2) Page 11-12, lines 245-246: It seems that authors interpret the bounce curves in a way that if the rebound fraction is 5%, approximately 5% of the particles are solid. Even the bounce curves for single components, such as sucrose, are s-shaped curves and rebound value varies between 1 and 0. In the case of sucrose particles all the particles have absorbed same amount of water at certain RH, hence they all have the same physical phase state. The reason why for example 20% of sucrose particles are bouncing off from the impactor is not because 20% of the particles are solid and 80% liquid. 20% of sucrose particles are bouncing off at certain RH and 80% are sticking on the impactor substrate because the velocity of particles in impactor jet depends on their radial distance from the center of the impactor jet. Hence in this example, 20% of sucrose particles have kinetic energy higher than the dissipation and surface adhesion energies. So it is obvious that increasing rebound fraction doesn't necessarily imply external mixture and increasing fraction of solid particles. It can also imply changes in material characteristics of all particles (more solid particles). This should be taken into account in data interpretation and also the text should be changed accordingly throughout the manuscript.

Thank you for this thoughtful comment. It is true that there is variation in the impact velocity and thus rebound fraction as a function of radial distance from the center of the impactor jet. We have modeled the flow-dynamics of our impactor and for the nozzles employed in this study (cf. Figure S3 and S4 of Bateman et al., 2014) and found the kinetic energy of the impacting particles at large diameters should be well above the adhesion energy even at high RH (cf. Figure 7 of the Bateman et al., 2014). This is the main reason for using particle diameters of 190 nm. Under the controlled conditions and thorough understanding of the particle flow dynamics of our impactor we can rule out any change in rebound fraction attributed to kinetic energy and surface adhesion.

We also agree that the reviewer is correct that we assume the particles are a homogeneous mixture during most of the analysis. To this point the caveat is included: *"…that increase viscosity when internally mixed with background PM and increased concentrations of non-liquid anthropogenic particles in external mixtures of anthropogenic and biogenic PM."* Overall, to the reviwer's point, the width of the rebound curve exceeds the width of calibration particles, indicating that there are different particle types undergoing nonliquid/liquid transitions at different RH values.

3) According to main conclusions of the paper the changes in measured rebound correlated with decreasing kappa and decreasing O:C. Still no data on O:C is shown in the whole manuscript. Authors should show, for example, how O:C varies between pollution, biomass burning and background cases and also during day and night (Figure 3). Also O:C panel should be added to figure 4.

The intention was to use PMF-A and PMF-B as the main supporting data for the changes in the measured rebound fractions. To avoid the confusion highlighted by the reviwer's comment, we removed the statement *"…decreasing O:C elemental ratios*," from the conclusions in the manuscript.

We addressed the reviewers concern that there is not enough data included for O:C ratios by adding Table S3 to the supporting information. This table includes the average O:C ratios for the various air mass classification categories and day/night time periods used in the manuscript. Text is added as follows: "*The average O:C ratios for the various air-mass classifications can be found in Table S3 of the Supplement."* The O:C panel is added to Figure 4.

4) Also the rebound data corresponding different cases (polluted-biomass burning background) should be shown.

These data sets are shown in Figure S1 as whisker-box plots. Test is added as follows, *"Figure S1 of the Supplement presents an additional level of detail."*

Anthropogenic influences on the physical state of submicron particulate matter over a tropical forest

Adam P. Bateman[1], Zhaoheng Gong[1], Tristan H. Harder[2], Suzane S. de Sá[1], Bingbing Wang[3,4], Paulo Castillo[5], Swarup China[3], Yingjun Liu[1], Rachel E. O'Brien[2,6], Brett B. Palm[7], Hung-Wei Shiu[3], Glauber G. Cirino[8], Ryan Thalman[5], Kouji Adachi[9], M. Lizabeth Alexander[3], Paulo Artaxo[10], Allan K. Bertram[11], Peter R. Buseck[12], Mary K. Gilles[2], Jose L. Jimenez[7], Alexander Laskin[3], Antonio O. Manzi[8], Arthur Sedlacek[5], Rodrigo A. F. Souza[13], Jian Wang[5], Rahul Zaveri[3], Scot T. Martin[*1,14]

[1]School of Engineering and Applied Sciences, Harvard University, Cambridge, Massachusetts, USA
[2]Chemical Sciences Division, Lawrence Berkeley National Laboratory, Berkeley, CA, USA
[3]William R. Wiley Environmental Molecular Sciences Laboratory, Pacific Northwest National Laboratory, Richland, WA, USA
[4]State Key Laboratory of Marine Environmental Science, College of Ocean and Earth Sciences, Xiamen University, Xiamen, China
[5]Brookhaven National Laboratory, Upton, New York, USA
[6]Department of Civil and Environmental Engineering, Massachusetts Institute of Technology, Cambridge, Massachusetts, USA
[7]University of Colorado, Boulder, USA
[8]National Institute of Amazonian Research, Amazonas, Brazil
[9]Atmospheric Environment and Applied Meteorology Research Department, Meteorological Research Institute, Tsukuba, Ibaraki, Japan
[10]University of São Paulo, São Paulo, Brazil
[11]Department of Chemistry, University of British Columbia, Vancouver, BC, Canada
[12]School of Earth and Space Exploration & School of Molecular Sciences, Arizona State University, Tempe, Arizona, USA
[13]Amazonas State University, Amazonas, Brazil
[14]Department of Earth and Planetary Sciences, Harvard University, Cambridge, Massachusetts, USA

Atmospheric Chemistry and Physics

[*] Correspondence to: S.T. Martin (scot_martin@harvard.edu)

Abstract

The occurrence of non-liquid and liquid physical states of submicron atmospheric particulate matter (PM) downwind of an urban region in central Amazonia was investigated. Measurements were conducted during two Intensive Operating Periods (IOP1 and IOP2) that took place during the wet and dry seasons, respectively, of the GoAmazon2014/5 campaign. Air masses representing variable influences of background conditions, urban pollution, and regional and continental scale biomass burning passed over the research site. As the air masses varied, particle rebound fraction, an indicator of physical state, was measured in real time at ground level using an impactor apparatus. Micrographs collected by transmission electron microscopy confirmed that liquid particles adhered while non-liquid particles rebounded. Relative humidity (RH) was scanned to collect rebound curves. When the apparatus RH matched ambient RH, 95% of the particles adhered as a campaign average. Secondary organic material, produced for the most part by the oxidation of volatile organic compounds emitted from the forest, produces liquid PM over this tropical forest. During periods of anthropogenic influence, by comparison, the rebound fraction dropped to as low as 60% at 95% RH. Analyses of the mass spectra of the atmospheric PM by positive-matrix factorization (PMF) and of concentrations of carbon monoxide, total particle number, and oxides of nitrogen were used to identify time periods affected by anthropogenic influences, including both urban pollution and biomass burning. The occurrence of non-liquid PM at high RH correlated with these indicators of anthropogenic influence. A linear model having as output the rebound fraction and as input the PMF factor loadings explained up to 70% of the variance in the observed rebound fractions. Anthropogenic influences can contribute to the presence of non-liquid PM in the atmospheric particle population through the combined effects of molecular species that increase viscosity when internally mixed

with background PM and increased concentrations of non-liquid anthropogenic particles in external mixtures of anthropogenic and biogenic PM.

1. Introduction

Particulate matter (PM) directly affects the Earth's climate by scattering and absorbing solar radiation and indirectly by effects on clouds (Ramanathan et al., 2001). The magnitude of these effects depends in part on the physical and chemical properties of the particulate matter (Andreae and Rosenfeld, 2008). The physical state of PM, as liquid or non-liquid, can influence the growth rates of small particles and ultimately the production of cloud condensation nuclei (CCN) (Riipinen et al., 2011;Perraud et al., 2012). Liquid particles pose negligible in-particle diffusion barriers for condensing species and therefore can grow rapidly. By comparison, non-liquid particles, referring to both semisolid and solid particles, can have a different behavior. For some conditions, semisolid particles can grow slowly because of in-particle limits on rates of molecular diffusion, and solid particles can grow even more slowly when limited to surface adsorption (Riipinen et al., 2012;Shiraiwa and Seinfeld, 2012;Li et al., 2015). Liquid compared to non-liquid PM can also affect reactivity (Kuwata and Martin, 2012;Li et al., 2015). The consequences of the differing growth mechanisms can be that the growth of small particles is relatively disfavored in a population of liquid particles of heterogeneous sizes, as compared to a similar population of non-liquid particles (Zaveri et al., 2014). An implication can be that CCN concentrations are ultimately greater for a population of non-liquid particles that grows to CCN sizes, as compared to a population of liquid particles.

Secondary organic material (SOM), produced by the oxidation of biogenic volatile organic compounds (BVOCs), is a major source of atmospheric PM, especially over forested regions where SOM often dominates the mass concentration of submicron PM (Hallquist et al., 2009;Jimenez et al., 2009). The physical state of SOM has been studied in both laboratory (Vaden et al., 2011;Kuwata and Martin, 2012;Perraud et al., 2012;Saukko et al., 2012;Renbaum-

87 Wolff et al., 2013;Kidd et al., 2014;Bateman et al., 2015;Li et al., 2015;Liu et al., 2015;Pajunoja
88 et al., 2015;Song et al., 2015) and ambient environments (Virtanen et al., 2010;O'Brien et al.,
89 2014;Bateman et al., 2016;Pajunoja et al., 2016). For background conditions of the Amazonian
90 tropical forest, a region dominated by isoprene-derived SOM and high RH, PM was mostly
91 liquid (Bateman et al., 2016). For a boreal forest in northern Europe, a region dominated by
92 pinene-derived SOM and low RH, PM was largely non-liquid (Virtanen et al., 2010). The
93 combined set of laboratory and ambient studies show that the physical state of PM having high
94 SOM content depends on the surrounding relative humidity (RH). This effect arises in part
95 because organic particles are hygroscopic to various extents depending on composition. Water
96 absorption, which is favored at elevated RH, has a plasticizing effect on physical state (Koop et
97 al., 2011).
98 The physical state of PM affected by urban pollution over forests remains largely
99 unexplored. A single day of ambient observations in central Amazonia suggested that ambient
100 PM affected by urban pollution tended toward a non-liquid state (Bateman et al., 2016), and
101 laboratory studies support the idea of an important modulating role of pollution in the physical
102 state of SOM. A non-liquid state was favored for SOM produced from single-ring aromatic
103 species (Liu et al., 2015;Song et al., 2015) as well as mixed with polycyclic aromatic
104 hydrocarbons (PAHs) (Zelenyuk et al., 2012;Abramson et al., 2013;Berkemeier et al., 2014).
105 Organic molecules associated with urban pollution and industrial activities tend to be less
106 hygroscopic than biogenic SOM (Hersey et al., 2013). When internally mixed within biogenic
107 SOM, the anthropogenic molecules have a tendency to reduce water uptake and thereby increase
108 the viscosity of the mixed particles. A similar line of reasoning leads to an identical hypothesis
109 for the effects of biomass burning emissions. Compared to prevailing background conditions of

SOM dominance over many forests, PM produced by biomass burning leads to a net effect of decreased water uptake when the PM mixes into the background particle population (Dusek et al., 2011).

The data sets presented herein provide observational evidence on the effects of anthropogenic influences on the physical state of ambient particulate matter. All other factors being equal, the lack of particle rebound is an indicator of liquid PM (Bateman et al., 2015). Conversely, the occurrence of particle rebound is an indicator of non-liquid PM. Rebounding and adhering particles were separately collected for conventional and chemical imaging. The data sets were collected during the two Intensive Operating Periods (IOP1 and IOP2) of the GoAmazon2014/5 experiment, corresponding to the wet and dry seasons, respectively (Martin et al., 2016). The research site (-3.2133°, -60.5987°), called "T3", was located 70 km downwind of the city of Manaus, population two million, in central Amazonia. Air masses representing background conditions, urban pollution, and regional and continental scale biomass burning passed over the research site. Herein, anthropogenic influence refers to all but background conditions. Under background conditions, the submicron PM in this region is dominated by biogenic SOM (Chen et al., 2009;Chen et al., 2015).

2. Experimental

An impactor apparatus was used for the study of particle rebound (Bateman et al., 2014;Bateman et al., 2015;Bateman et al., 2016; Li et al., 2016). The apparatus was housed inside a temperature-controlled research trailer at the T3 site. Particulate matter was sampled at 5 m above ground through copper tubing having an outer diameter of 13 mm (0.5 inch). In sequence, a drying unit reduced the sampled flow to 25% RH or lower, a Differential Mobility Analyzer (DMA, TSI 3085) selected a subpopulation of dried particles having a narrow

distribution of electric mobility, and a humidification unit (Nafion tubes; Perma Pure, MD 110) elevated the RH of the mobility-filtered flow to the targeted RH of a measurement. The drying unit consisted of a Nafion drier in series with a silica gel diffusion drier, and the silica gel was replaced every two days. After passing the dryer, DMA, and humidifier, the resulting flow was split and passed through three impactors operated in parallel. Labels *i*, *ii*, and *iii* refer to each of the three impactors. Each impactor was operated at a flow rate of 1.0 Lpm, corresponding to a setpoint aerodynamic diameter d_a^* of 84.9 ± 5.4 nm (Bateman et al., 2014). Particle number concentrations, denoted by N_i, N_{ii}, or N_{iii}, exiting the impactors were measured by three independent condensation particle counters (CPC, TSI 3010). Measurements were conducted from February 14 to March 16, 2014, during IOP1 and from September 4 to October 15, 2014, during IOP2.

The three impactors differed from one another by having uncoated, coated, or no impaction plate. The impactor having the uncoated plate passed both non-impacted and rebounded particles. The impactor having the coated plate (Dow Corning High-Vacuum Grease) passed only non-impacting particles. The impactor having no plate passed all particles. Its purpose was to serve as a compensation arm for possible miscellaneous particle losses, such as wall loss. Based on the particle number concentrations measured downstream of the impactors, the rebound fraction was calculated as follows (Bateman et al., 2014):

$$f = \frac{N_i - N_{ii}}{N_{iii} - N_{ii}} \quad (1)$$

The terms N_i, N_{ii}, and N_{iii} represent the particle number concentration measured downstream of the impactors having uncoated, coated, and no impaction plate, respectively. The standard

deviation of the rebound fraction was based on error propagation for an uncertainty in N of $N^{-1/2}$ (Agarwal and Sem, 1980).

A rebound curve representing f(RH) constituted an individual data set. For most measurements, the DMA setting for electric mobility was held constant (typically 190 nm), the RH in the humidification unit was changed stepwise every few minutes, and f was continuously recorded. Additional protocols of DMA settings and RH profiles were used in a few cases. All protocols, including differences between IOP1 and IOP2, are described in Section S1 of the Supplement.

In conjunction with the rebound measurements, particles were collected for imaging by transmission electron microscopy (TEM) and scanning transmission X-ray microscopy (STXM). Images in some cases can directly suggest the liquid or non-liquid state of individual particles (O'Brien et al., 2014;Wang et al., 2016). Samples for imaging were collected as follows. A fourth impactor was added in parallel with the other three impactors. Imaging substrates were affixed to the impaction plate, and multiple substrates were mounted to the plate for concurrent collection for the various microscopy techniques. Substrates included grids coated with Formvar (EMJapan Co., Tokyo, Japan) or lacey carbon (Ted Pella Inc., USA) for TEM and silicon nitride membrane windows (Silson, UK) for STXM. The flow rate and setpoint aerodynamic diameter of the fourth impactor were the same as for the other three impactors. The collected particles represented those that adhered to the substrate at impact, and an assumption in the analysis is that rebound from the substrate was similar to that from the uncoated plate. The flow through this fourth impactor was pulled by an in-line TEM autosampler (Arios Inc., Tokyo, Japan (Adachi et al., 2014)). In this way, the setup separately collected particles that adhered to the grids on the impaction plate and particles that rebounded from the impaction plate and passed to the

177 autosampler. The autosampler collected particles having aerodynamic diameters from 60 to 350
178 nm. Particles adhered to the TEM substrates in the autosampler yet rebounded from the TEM
179 substrates in the impactor because of the significantly different particle impact velocities
180 between the two impactors (i.e., cut-point and impactor design). Samples were collected for
181 TEM analysis between September 30 and October 15, 2014. Samples were collected for STXM
182 analysis between 1:00 and 10:00 (UTC) on October 1, 2014.

183 Microanalysis of individual particles of the collected PM was performed using two
184 instruments: (1) a transmission electron microscope (TEM; JEOL, JEM-1400) equipped with an
185 energy-dispersive X-ray spectrometer (EDS; Oxford Instruments) and (2) a scanning
186 transmission X-ray microscope interfaced for near-edge X-ray absorption fine structure
187 spectroscopy (STXM/NEXAFS; Advanced Light Source, Berkeley). For TEM, imaging was by
188 bright-field microscopy, and particle composition was investigated by EDS. For STXM, at a
189 fixed photon energy an image was obtained by detecting the transmitted light at each pixel while
190 raster scanning the sample. Spatially resolved NEXAFS spectra were obtained from a set of
191 images recorded at different photon energies. The NEXAFS spectra provided chemical bonding
192 information and quantitative elemental ratios (Moffet et al., 2010a;Moffet et al., 2010b;O'Brien
193 et al., 2014;Piens et al., 2016). Section S2 of the Supplement presents further technical
194 information concerning the TEM and STXM/NEXAFS analyses.

195 Additional co-located measurements used in the data analysis herein included a High-
196 Resolution Time-of-Flight Aerosol Mass Spectrometer (AMS; Aerodyne Inc.), a Single-Particle
197 Soot Photometer (SP2; Droplet Measurement Technologies), a size-resolved Cloud
198 Condensation Nuclei Counter (CCNC; Droplet Measurement Technologies, CCNC-100), a
199 Condensation Particle Counter (TSI, CPC 3772) for measuring particle number concentrations,

an Integrated Cavity Output Spectroscope (ICOS; Los Gatos) for measuring carbon monoxide (CO) concentration, and a Trace Level Enhanced detector (TLE; Thermo Scientific, Model 42i, with further customization) for the measuring concentrations of nitrogen oxides (NO_y). The latter three instruments were deployed at the T3 site as part of the USA Department of Energy (DOE) Atmospheric Radiation Measurement (ARM) Climate Research Facility, including the ARM Mobile Facility One (AMF-1) and the Mobile Aerosol Observing System (MAOS) (Mather and Voyles, 2013;Martin et al., 2016). This facility also collected the meteorological data used herein, including temperature, relative humidity, wind direction, and wind speed. The AMS measured the chemical composition in real-time of non-refractory submicron particles (DeCarlo et al., 2006). The high-resolution data of the organic component in "V-mode" was used in conjunction with positive-matrix factorization (PMF) analysis (Ulbrich et al., 2009) to obtain statistical factors and the associated time series of factor loadings for each season (de Sá et al., 2016). As a surrogate for concentrations of black carbon, the SP2 measured the time-resolved scattering and incandescence produced by irradiated refractory, light-absorbing components of individual particles having volume-equivalent diameters between 70 and 600 nm (Schwarz et al., 2006;Moteki and Kondo, 2007). The size-resolved CCN activity was obtained by classifying dry particles using a DMA (TSI 3081) and then exposing them successively to a range of supersaturations inside the CCNC (Thalman et al., in preparation). The hygroscopicity and CCN activity were analyzed via κ-Köhler theory, which relates particle critical supersaturation to the initial dry diameter and hygroscopicity (Petters and Kreidenweis, 2007;Petters et al., 2009).

3. Results and Discussion

3.1 *Rebound Observations*

Particle rebound or particle adhesion at impact depends on the balance of energies. Particle rebound occurs when the kinetic energy before impact is greater than the sum of dissipation and surface adhesion energies after impact (Tsai et al., 1990;Bateman et al., 2014). The dissipation energy of liquid particles is much greater than that of solid particles because of additional mechanisms of dissipation available to the former. As a point of reference, the transition from rebound to adhesion occurs across a viscosity transition of 10^2 to 1 Pa s for sucrose particles for the operating conditions of the impactor (Bateman et al., 2015). The viscosity range corresponding to the rebound transition can depend on particle composition, but this aspect is not investigated herein.

The rebound curves of particles of 190-nm mobility diameter are shown in Figure 1a for IOP1 and IOP2. For RH < 50%, the rebound fraction was between 0.8 and 1.0. For RH > 50%, the rebound fraction decreased monotonically to a low value, typically zero. The shape of the rebound curve in Figure 1a is similar to that for particles of secondary organic material produced in the Harvard Environmental Chamber (Bateman et al., 2015). The rebound fraction of SOM particles produced from isoprene or α-pinene became zero for RH > 90%.

The subset of the data for which the apparatus RH matched the ambient RH is shown in Figure 1b (cf. Section S3 of Supplement). In light of the distribution of ambient RH values (cf. Figure 1c), the data set in Figure 1b implies that submicron PM in this tropical environment was liquid most of the time. Bateman et al. (2016) reported such a result for observations under background conditions at this site for data sets collected in 2013 a few months before GoAmazon2014/5 began. The present results reported for GoAmazon2014/5 represent a longer

time series (i.e., 550 compared to 30 rebound curves) and reinforce the generality of the earlier result of Bateman et al. (2016) of the prevalence of liquid PM for this forested region under background conditions.

In the larger set of observations of the present study, what also emerges is that the rebound fraction remained in median at 0.05 even at 95% RH, implicating the presence of externally mixed PM in the atmosphere. Approximately 5% of the particles were non-liquid even to 95% RH in both the wet and dry seasons (i.e., IOP1 and IOP2) (Figures 1a and 1b). At times, rebound fractions of up to 0.4 occurred for RH > 90%. Elevated rebound fractions were observed more frequently in IOP2 than IOP1. During IOP2, which was extensively influenced by biomass burning, non-liquid particles in median constituted a fraction of 0.3 at 70% RH and a fraction of 0.1 at 90%. These RH values prevailed approximately 10% of the time. Events of elevated rebound fraction were associated with the pollution plume from Manaus during IOP1 in the wet season and with both this urban plume as well as increased regional biomass burning during IOP2 in the dry season (cf. Section 3.2).

Probability density functions (PDF) of rebound fraction at 75% RH based on the data sets of Figure 1a are shown in Figure 2 for (a) IOP1 and (b) IOP2 for three types of air masses during day and night time periods. Daytime represents 12:00 to 16:00 (local time) (16:00 to 20:00 UTC) and nighttime represents 23:00 to 04:00 (local time) (03:00 to 08:00 UTC). Air masses were identified as background, as influenced by local to regional biomass burning, or as influenced by Manaus pollution. The classification scheme was based on concentration regimes of particle number, carbon monoxide, and odd nitrogen (NO_y), as presented in Section S4 of the Supplement. Background conditions included contributions both from natural processes and from the long-distance transport and extensive oxidation of biomass burning emissions (Chen et

al., 2009;Martin et al., 2010). Natural processes in this region were dominated by the production of secondary organic material from oxidation of plant emissions (Martin et al., 2010;Poschl et al., 2010). Figure 2a shows that the mode value of the PDF shifted higher under the influence of Manaus pollution compared to background conditions, meaning that rebound became more probable and indicating an increasing presence of non-liquid PM at 75% RH. In Figure 2b, the mode value shifted even higher under the influence of biomass burning. For each type of air mass, the nighttime mode values were higher than the daytime equivalents. The day-night differences were lowest under background conditions.

The increase in rebound at night might be explained by a combination of interacting factors. A shallow stable nocturnal boundary layer can trap and thereby concentrate anthropogenic non-liquid particles emitted at night from local emissions, including smoldering fires during IOP2. During the day, the boundary layer expands and dilution is more effective. In addition, the production of liquid secondary organic material by biogenic processes is comparatively more rapid.

For further analysis, the rebound curves recorded under background conditions were averaged separately for IOP1 and IOP2 (cf. Figure 1a and Section S5 of the Supplement). These two background-average curves served as references against which deviations in rebound fraction were calculated for all air masses. Rebound deviation represents the excess non-liquid PM over background conditions after detrending the data for the dependence on relative humidity. The rebound deviations for IOP1 and IOP2 are plotted in Figure 3. Rebound deviations as high as +0.5 in rebound fraction were observed. Statistics of Figure 3 are summarized in Table S1, including for the subset of measurements matched with the ambient RH. For the full set of data, including the full range of RH, rebound deviations greater than 0.1 represented 17% and

35% of the observations during IOP1 and IOP2, respectively. These deviations, corresponding to increased rebound and thus indicating an increasing presence of non-liquid PM, corresponded to the anthropogenic influences, as developed further in Section 3.2.

3.2 *Relationships between Rebound and Other Observations*

3.2.1 Case Studies

Transitions between background and polluted conditions across 24 hour-periods are presented in Figure 4 as representative examples for each IOP. The bottom panel shows the deviation in rebound fraction relative to the background-average curve (cf. Section S5 of Supplement). Color coding distinguishes relative humidity. From bottom to top, other panels in the figure show temperature, wind direction, wind speed, relative fractions of two groups of AMS PMF factor loadings, black carbon (BC) concentration, sulfate concentration, and total submicron PM mass concentration. Processes contributing to the loading of PMF group A are largely associated with the background atmosphere of Amazonia, including the possibility of long-range transport and extensive oxidation of biomass burning emissions. Processes contributing to the loading of PMF group B are largely associated with urban pollution and local and regional biomass burning (cf. Section S6 of Supplement).

Shifts in the deviation in the rebound fraction from the background-average curve are apparent in the time series in the bottom panels of Figure 4. At these times, the fractional loading of PMF group A decreased and that of PMF group B increased, indicating a shift away from background conditions. Background conditions were characterized by high loadings of PMF group A and small rebound deviations. In the left panel (IOP1), in an example of one type of an anthropogenic event, black carbon concentration and the fractional loading of PMF group B abruptly increased together. The rebound deviation simultaneously increased, indicating an

312 increasing presence of non-liquid PM, especially above 70% RH. In the right panel (IOP2), in an
313 example of a second type of an anthropogenic event, the background air mass was gently
314 replaced by an air mass characterized by small increases in rebound deviation and fractional
315 loading of PMF group B yet lacking an associated increase in black carbon concentration. In an
316 example of a third type of anthropogenic event, this air mass was later replaced by an air mass
317 characterized by a strong increase in the fractional loading of PMF group B, total PM mass
318 concentration, and rebound deviation. Around 15:00 (UTC), a convective event associated with
319 rainfall decreased temperature, changed wind direction, and increased wind velocity, and
320 background conditions returned.

321 TEM images collected during the time periods of elevated rebound corroborate the
322 foregoing interpretation of liquid and non-liquid PM for adhering compared to rebounding
323 particles. Images of particles that adhered to the TEM substrates in the impactor at 95% RH are
324 shown in Figure 5a. The images were taken at a tilt angle of 60° so that the aspect ratio of the
325 particles could be viewed. The images show that most adhering particles spread out across the
326 substrate, indicating flattening upon impact, as expected for liquid particles. Some of these
327 adhering particles had a mixed composition, appearing as solid cores surrounded by halos of
328 flattened liquid shells. The horizontal dimensions of the flattened particles approached 1 to 2 μm
329 for vertical dimensions of tens of nanometers. Pöschl et al. (2010) previously recorded similar
330 images for ambient particles in the wet season of 2008 in central Amazonia during the
331 Amazonian Characterization Experiment (AMAZE-08) (Martin et al., 2010). For comparison to
332 the images of the adhering particles, images of particles that rebounded at 95% RH from the
333 impaction plate are shown in Figure 5b. These particles were collected downstream of the
334 impactor. The images show that these particles had high vertical dimensions and spherical or

dome-like morphologies and thus suggest that the particles experienced little deformation upon impact, as expected for solid particles.

3.2.2 Descriptive Statistics

The results of Figures 3 and 4 are further analyzed in Figure 6. Statistics of rebound deviation are shown by box-whisker representation for different windows of relative humidity Figure S1 of the Supplement presents an additional level of detail. The data sets were segregated for presentation by IOP1/IOP2, daytime/nighttime, and air mass type. For background conditions, the rebound deviations relative to their average were mostly zero, indicating that there was low variability among different background air masses. The exception was for the night periods of IOP1. By comparison, under anthropogenic influences, the rebound deviation was positive for both IOPs. Positive deviations were most significant between 65% and 95% RH. In all cases, the nighttime deviations were greater than the daytime counterparts. For IOP2, the prevalence of biomass burning confounded separate classifications of urban pollution and biomass burning, and a classification of biomass burning took precedent. Rebound deviations were strongest during these time periods. Statistics of the analysis are further summarized in Table S2 (cf. Section S7 of Supplement). The average O:C ratios for the various air-mass classifications can be found in Table S3 of the Supplement.

3.2.3 Statistical correlations

Scatter plots of rebound deviation with environmental variables of ambient temperature, wind speed, and wind direction show no correlation for both daytime and nighttime datasets (cf. Figure S2 of the Supplement). Scatter plots of rebound deviation with some possible anthropogenic influences are presented in Figure S3. Soot, typically characterized by a solid core region of black carbon, is expected in abundance both in urban pollution and biomass burning

358 emissions. There was, however, no correlation between rebound deviation and black carbon
359 concentrations. There was also no correlation between rebound deviation and total particle mass
360 concentration. Rebound deviation and sulfate concentration weakly anti-correlated, which might
361 be expected given the hygroscopicity of sulfate. Sulfate concentrations, however, were a poor
362 indicator of anthropogenic influence in this region because the variability in background
363 concentrations was comparable in magnitude to any urban influence(de Sá et al., 2016). As a
364 caveat, an assumption in correlation tests is that variance arises from a single variable, and the
365 possibility of two or more contributing or interacting factors is not directly considered.

366 Given that water uptake is an important process for softening organic material, scatter
367 plots of the rebound deviation at 75% RH with the hygroscopicity parameter κ are shown in
368 Figures 7a and 7b for the data sets from IOP1 and IOP2, respectively. Lower values of κ
369 represent decreased equilibrium water uptake for a fixed RH (Petters and Kreidenweis, 2007).
370 The plots show that the rebound deviation increased as the κ value decreased, meaning that
371 particles of lower hygroscopicity were less prone to being in liquid form.

372 The apparent shift to higher κ values from IOP1 to IOP2 might be explained by
373 instrumental methods. During IOP1, κ values were measured using the impactor apparatus at
374 sub-saturated RH (i.e., < 100%) (cf. Section S8 of the Supplement). During IOP2, κ values were
375 measured using a size-resolved CCN instrument at super-saturated RH (i.e., > 100%) (Thalman
376 et al., in preparation). Sub- and supersatured κ values can be systematically different (Petters and
377 Kreidenweis, 2007; Ruehl et al., 2016).

378 3.2.4 Chemical characteristics of rebounded particles

379 An analysis of the relationship between rebound deviation and chemical characteristics is
380 presented in Figure 8 based on the fractional loading of PMF group B. The data sets are

segregated for presentation by IOP1/IOP2, daytime/nighttime, and four bands of fractional loading. Within each panel, box-whisker statistics of rebound deviation are shown for different windows of relative humidity, ranging from 50% to 95%. The figure shows that the rebound deviation increased at all RH values as the fractional loading of group B increased. The background-average curve used as the reference for rebound deviation corresponded to a fractional loading of 0.00 to 0.15 for group B or correspondingly of 0.85 to 1.00 for group A. An increasing fractional loading of group B represented greater anthropogenic influence. The inference is that anthropogenic influences, represented by a combination of urban pollution and biomass burning, affected chemical composition in ways that increased the presence of non-liquid PM above 50% RH.

Scatter plots between rebound deviation at 75% RH and the fractional loading of group B are shown in Figures 9a and 9b for the data sets of the two IOPs. The data points are colored according to the value of the hygroscopicity parameter κ. The plots show that rebound deviation increased for low hygroscopicity and high fractional loading of group B, in agreement with the presentation in Figures 7a and 7b and Figure 8. Figures 9a and 9b further show in explicit fashion that the highest rebound deviations occurred during time periods affected by biomass burning and urban pollution, as characterized by the lowest values of κ and the highest fractional loadings of group B. Smaller κ values for lower fractional loadings of group B can be explained by the differences in O:C ratios between group A and B (Massoli et al., 2010): the O:C ratios were 0.95/0.95 (IOP1/IOP2) and 0.42/0.54 for groups A and B, respectively.

A model to predict rebound deviation based on chemical characteristics was constructed. The fractional loadings of PMF group A and B were used as model inputs, and model coefficients represented the effects of RH across nine bands (cf. Section S9 of the Supplement).

The observed and predicted rebound deviations are plotted in Figure 10. The corresponding coefficients R^2 of determination were 0.65 and 0.72 for IOP1 and IOP2, respectively. Predicted values were biased high for low rebound deviation and biased low for high rebound deviation. The magnitudes of the model coefficients represented the relative importance of the two PMF groups in predicting rebound deviation (Table S5). In this regard group B dominated during both IOPs. This result is consistent with the role of anthropogenic influences in shifting the PM population to fewer liquid particles and more non-liquid particles.

Analysis by STXM/NEXAFS supports the foregoing narrative of anthropogenic influence as a modulator between liquid and non-liquid PM. Rebounded particles were collected on October 1 during a time period classified as influenced by biomass burning emissions. The carbon K-edge spectrum is shown in Figure 11a, and the STXM image is shown in Figure 11b. A notable feature of the NEXAFS spectrum of the rebounded particles is the strong double bond. Pöhlker et al. (2012) previously collected NEXAFS spectra for samples collected at a background site in central Amazonia, and the strong feature of a double bond was absent. The spectra instead resembled those of different types of reference biogenic secondary organic material.

For comparison to the spectrum collected of the rebounded particles, carbon K-edge spectra are shown for carbonaceous particles collected in other field and laboratory studies. Based on these results as well as those of the rebound measurements, a hypothesis of soot or black carbon to explain the rebounding particles was ruled out on three grounds. The double-bond feature was homogeneously distributed throughout the particles (Figure 11b) compared to inclusions that are typical for soot (Moffet et al., 2013;Knopf et al., 2014;O'Brien et al., 2014), rebound deviation and black carbon concentrations did not correlate (Figure S3), and the

spectroscopic signatures of rebounded particles and soot did not match (Figure 11a). A hypothesis of VOC-derived secondary organic material, including possible changes because of shifts from HO_2 to NO-dominant chemistry (Liu et al., 2016a;Liu et al., 2016b), was also eliminated by comparison of the NEXAFS spectrum of the rebounded particles to the reference spectra for laboratory samples. An important caveat to these interpretations is that some of the hypotheses ruled out for this particular day might still have a role to play on other days.

There was exceptional uniformity in the particle population characterized by STXM/NEXAFS, which could suggest that the rebounding PM represented distant sources or alternatively a strong single nearby source. The gray region around the red line in Figure 11a illustrates the low variability across the population of analyzed particles (Figure 11b). Moreover, the variability in the O:C ratio determined by the NEXAFS analysis was just ± 0.01 for O:C = 0.34 (± 0.03) [± 0.01], where the value in parentheses was the uncertainty of the measurement and the value in the bracket was the variability across the image in Figure 11b. During the same time period, the O:C ratio of the ambient PM was 0.77 ± 0.04 by AMS measurements. Hence, the rebounding particles were significantly less oxidized, as consistent with increased double bond (C=C) content and increased fractional loading of PMF group B.

Several speculations can be made for the origins of the particles leading to the data set of October 1. The chemical constituents giving rise to the double bonds might derive from biological degradation products from incomplete combustion, such as in biomass burning (Tivanski et al., 2007;Keiluweit et al., 2010). Unexplained by this speculation, however, is the absence of a potassium signature in the NEXAFS spectra, which is typical of most biomass burning. Future collection of NEXAFS spectra would be well motivated for the several different types of biomass burning in an Amazonian context, such as from nearby fields, regionally around

Manaus, two or three days away from other regions of South America, and up to a week away from Africa. An alternative speculation for this data set is that solid organic particles produced by the impact of raindrops on wet soil surfaces could be making a contribution to the rebounded PM analyzed here (Joung and Buie, 2015). Wang et al. (2016) recently reported detection of the airborne soil organic particles generated by this mechanism over agricultural fields in the central plains of the USA, and the corridor from Manaus to T3 has many agricultural fields. The rebounded particles collected at T3 and the agricultural particles reported in Wang et al. (2016) both had a homogeneous distribution of double bonds and similar elemental ratios and absorption features. Even so, preliminary analysis across the extended data set at T3 between rebound and nearby precipitation did not show a clear correlation. Another speculation relates to the importance of aromatic compounds as hardening agents. Several gas-phase aromatic compounds, laden with double bonds, were measured during IOP1 and IOP2, including toluene, benzene, trimethylbenzene, and xylenes by proton-transfer mass spectrometry (Liu et al., 2016b). Rebound deviation correlated positively with the concentrations of these compounds during both IOPs, and the correlation was stronger during the night. Laboratory studies show that the uptake of polycyclic aromatic hydrocarbons during the formation of biogenic PM can increase the viscosity of the PM (Vaden et al., 2011;Zelenyuk et al., 2012;Abramson et al., 2013;Liu et al., 2015).

4. Conclusions

Under background conditions, particles composed primarily of highly-oxidized biogenic PM were hygroscopic, and they were liquid for the RH values prevailing over Amazonia at surface level. Anthropogenic influences of urban pollution and biomass burning decreased hygroscopicity, and non-liquid PM became more favored. The shift in physical state correlated

with increasing concentrations of C=C functionalities and increasing fractional loadings of AMS PMF group B, both of which were indicative of anthropogenic influences. These results demonstrate the importance of anthropogenic influences for altering the physical properties of ambient particulate matter over tropical forests.

Acknowledgments. Institutional support was provided by the Central Office of the Large Scale Biosphere Atmosphere Experiment in Amazonia (LBA), the National Institute of Amazonian Research (INPA), and Amazonas State University (UEA). The Office of Biological and Environmental Research of the Office of Science of the United States Department of Energy is acknowledged for funding, specifically the Atmospheric Radiation Measurement (ARM) Climate Research Facility, the Atmospheric System Research (ASR) Program, the Division of Chemical Sciences, Geosciences, and Biosciences (Advanced Light Source at Lawrence Berkeley National Laboratory, Beamlines 5.3.2 and 11.0.2), the Environmental Molecular Sciences Laboratory (EMSL), and Pacific Northwest National Laboratory (PNNL). Further funding was provided by the Amazonas State Research Foundation (FAPEAM), the São Paulo State Research Foundation (FAPESP), the Brazil Scientific Mobility Program (CsF/CAPES), the USA National Science Foundation, and the Japanese Ministry of the Environment. The work was conducted under scientific licenses 001030/2012-4 of the Brazilian National Council for Scientific and Technological Development (CNPq).

References

Abramson, E., Imre, D., Beranek, J., Wilson, J., and Zelenyuk, A.: Experimental determination of chemical diffusion within secondary organic aerosol particles, Phys. Chem. Chem. Phys., 15, 2983-2991, 10.1039/c2cp44013j, 2013.

Adachi, K., Zaizen, Y., Kajino, M., and Igarashi, Y.: Mixing state of regionally transported soot particles and the coating effect on their size and shape at a mountain site in japan, J. Geophys. Res. Atmos., 119, 5386-5396, 10.1002/2013jd020880, 2014.

Agarwal, J. K., and Sem, G. J.: Continuous-flow, single-particle-counting condensation nucleus counter, J. Aerosol Sci, 11, 343-&, 10.1016/0021-8502(80)90042-7, 1980.

Andreae, M. O., and Rosenfeld, D.: Aerosol-cloud-precipitation interactions. Part 1. The nature and sources of cloud-active aerosols, Earth Sci. Rev., 89, 13-41, 10.1016/j.earscirev.2008.03.001, 2008.

Bateman, A. P., Belassein, H., and Martin, S. T.: Impactor apparatus for the study of particle rebound: Relative humidity and capillary forces, Aerosol Sci. Technol., 48, 42-52, 10.1080/02786826.2013.853866, 2014.

Bateman, A. P., Bertram, A. K., and Martin, S. T.: Hygroscopic influence on the semisolid-to-liquid transition of secondary organic materials, J. Phys. Chem. A, 119, 4386-4395, 10.1021/jp508521c, 2015.

Bateman, A. P., Gong, Z., Liu, P., Sato, B., Cirino, G., Zhang, Y., Artaxo, P., Bertram, A. K., Manzi, A. O., Rizzo, L. V., Souza, R. A. F., Zaveri, R. A., and Martin, S. T.: Sub-micrometre particulate matter is primarily in liquid form over Amazon rainforest, Nature Geosci, 9, 34-37, 10.1038/ngeo2599, 2016.

Brechtel, F. J., and Kreidenweis, S. M.: Predicting particle critical supersaturation from hygroscopic growth measurements in the humidified TDMA. Part I: Theory and sensitivity studies, Journal of the Atmospheric Sciences, 57, 1854-1871, 10.1175/1520-0469(2000)057<1854:ppcsfh>2.0.co;2, 2000.

Chen, Q., Farmer, D. K., Schneider, J., Zorn, S. R., Heald, C. L., Karl, T. G., Guenther, A., Allan, J. D., Robinson, N., Coe, H., Kimmel, J. R., Pauliquevis, T., Borrmann, S., Poschl, U., Andreae, M. O., Artaxo, P., Jimenez, J. L., and Martin, S. T.: Mass spectral characterization of submicron biogenic organic particles in the Amazon basin, Geophys. Res. Lett., 36, L20806, 10.1029/2009gl039880, 2009.

Chen, Q., Farmer, D. K., Rizzo, L. V., Pauliquevis, T., Kuwata, M., Karl, T. G., Guenther, A., Allan, J. D., Coe, H., Andreae, M. O., Pöschl, U., Jimenez, J. L., Artaxo, P., and Martin, S. T.: Submicron particle mass concentrations and sources in the Amazonian wet season (AMAZE-08), Atmos. Chem. Phys., 15, 3687-3701, 10.5194/acp-15-3687-2015, 2015.

de Sá, S. S., Palm, B. B., Campuzano-Jost, P., Day, D. A., Newburn, M. K., Hu, W., Isaacman-VanWertz, G., Yee, L. D., Thalman, R., Brito, J., Carbone, S., Artaxo, P., Goldstein, A. H., Manzi, A. O., Souza, R. A. F., Mei, F., Shilling, J. E., Springston, S. R., Wang, J., Surratt, J. D., Alexander, M. L., Jimenez, J. L., and Martin, S. T.: Influence of urban pollution on the production of organic particulate matter from isoprene epoxydiols in central amazonia, Atmos. Chem. Phys. Discuss., 2016, 1-58, 10.5194/acp-2016-1020, 2016.

DeCarlo, P. F., Kimmel, J. R., Trimborn, A., Northway, M. J., Jayne, J. T., Aiken, A. C., Gonin, M., Fuhrer, K., Horvath, T., Docherty, K. S., Worsnop, D. R., and Jimenez, J. L.: Field-deployable, high-resolution, time-of-flight aerosol mass spectrometer, Anal. Chem., 78, 8281-8289, 10.1021/ac061249n, 2006.

Dusek, U., Frank, G. P., Massling, A., Zeromskiene, K., Iinuma, Y., Schmid, O., Helas, G., Hennig, T., Wiedensohler, A., and Andreae, M. O.: Water uptake by biomass burning aerosol at sub- and supersaturated conditions: Closure studies and implications for the role of organics, Atmos. Chem. Phys., 11, 9519-9532, 10.5194/acp-11-9519-2011, 2011.

Hallquist, M., Wenger, J. C., Baltensperger, U., Rudich, Y., Simpson, D., Claeys, M., Dommen, J., Donahue, N. M., George, C., Goldstein, A. H., Hamilton, J. F., Herrmann, H., Hoffmann, T., Iinuma, Y., Jang, M., Jenkin, M. E., Jimenez, J. L., Kiendler-Scharr, A., Maenhaut, W., McFiggans, G., Mentel, T. F., Monod, A., Prevot, A. S. H., Seinfeld, J. H., Surratt, J. D., Szmigielski, R., and Wildt, J.: The formation, properties and impact of secondary organic aerosol: Current and emerging issues, Atmos. Chem. Phys., 9, 5155-5236, 10.5194/acp-9-5155-2009, 2009.

Hersey, S. P., Craven, J. S., Metcalf, A. R., Lin, J., Lathem, T., Suski, K. J., Cahill, J. F., Duong, H. T., Sorooshian, A., Jonsson, H. H., Shiraiwa, M., Zuend, A., Nenes, A., Prather, K. A., Flagan, R. C., and Seinfeld, J. H.: Composition and hygroscopicity of the los angeles aerosol: Calnex, Journal of Geophysical Research: Atmospheres, 118, 3016-3036, 10.1002/jgrd.50307, 2013.

Jimenez, J. L., Canagaratna, M. R., Donahue, N. M., Prevot, A. S. H., Zhang, Q., Kroll, J. H., DeCarlo, P. F., Allan, J. D., Coe, H., Ng, N. L., Aiken, A. C., Docherty, K. S., Ulbrich, I. M., Grieshop, A. P., Robinson, A. L., Duplissy, J., Smith, J. D., Wilson, K. R., Lanz, V. A., Hueglin, C., Sun, Y. L., Tian, J., Laaksonen, A., Raatikainen, T., Rautiainen, J., Vaattovaara, P., Ehn, M., Kulmala, M., Tomlinson, J. M., Collins, D. R., Cubison, M. J., Dunlea, E. J., Huffman, J. A., Onasch, T. B., Alfarra, M. R., Williams, P. I., Bower, K., Kondo, Y., Schneider, J., Drewnick, F., Borrmann, S., Weimer, S., Demerjian, K., Salcedo, D., Cottrell, L., Griffin, R., Takami, A., Miyoshi, T., Hatakeyama, S., Shimono, A., Sun, J. Y., Zhang, Y. M., Dzepina, K., Kimmel, J. R., Sueper, D., Jayne, J. T., Herndon, S. C., Trimborn, A. M., Williams, L. R., Wood, E. C., Middlebrook, A. M., Kolb, C. E., Baltensperger, U., and Worsnop, D. R.: Evolution of organic aerosols in the atmosphere, Science, 326, 1525-1529, 10.1126/science.1180353, 2009.

Joung, Y. S., and Buie, C. R.: Aerosol generation by raindrop impact on soil, Nature Communications, 6, 10.1038/ncomms7083, 2015.

Keiluweit, M., Nico, P. S., Johnson, M. G., and Kleber, M.: Dynamic molecular structure of plant biomass-derived black carbon (biochar), Environ. Sci. Technol., 44, 1247-1253, 10.1021/es9031419, 2010.

Kelly, W. P., and McMurry, P. H.: Measurement of particle density by inertial classification of differential mobility analyzer generated monodisperse aerosols, Aerosol Sci. Technol., 17, 199-212, 10.1080/02786829208959571, 1992.

Kidd, C., Perraud, V., Wingen, L. M., and Finlayson-Pitts, B. J.: Integrating phase and composition of secondary organic aerosol from the ozonolysis of α-pinene, Proc. Natl. Acad. Sci. U. S. A., 111, 7552-7557, 10.1073/pnas.1322558111, 2014.

Knopf, D. A., Alpert, P. A., Wang, B., O'Brien, R. E., Kelly, S. T., Laskin, A., Gilles, M. K., and Moffet, R. C.: Microspectroscopic imaging and characterization of individually identified ice

nucleating particles from a case field study, J. Geophys. Res. Atmos., 119, 10.1002/2014jd021866, 2014.

Koop, T., Bookhold, J., Shiraiwa, M., and Poschl, U.: Glass transition and phase state of organic compounds: Dependency on molecular properties and implications for secondary organic aerosols in the atmosphere, Phys. Chem. Chem. Phys., 13, 19238-19255, 10.1039/c1cp22617g, 2011.

Kuwata, M., and Martin, S. T.: Phase of atmospheric secondary organic material affects its reactivity, Proc. Natl. Acad. Sci. U. S. A., 109, 17354-17359, 10.1073/pnas.1209071109, 2012.

Li, Y. J., Liu, P. F., Gong, Z. H., Wang, Y., Bateman, A. P., Bergoend, C., Bertram, A. K., and Martin, S. T.: Chemical reactivity and liquid/nonliquid states of secondary organic material, Environ. Sci. Technol., 49, 13264-13274, 10.1021/acs.est.5b03392, 2015.

Liu, P., Li, Y. J., Wang, Y., Gilles, M. K., Zaveri, R. A., Bertram, A. K., and Martin, S. T.: Lability of secondary organic particulate matter, Proc. Natl. Acad. Sci. U. S. A., 113, 12643-12648, 10.1073/pnas.1603138113, 2016a.

Liu, P. F., Abdelmalki, N., Hung, H. M., Wang, Y., Brune, W. H., and Martin, S. T.: Ultraviolet and visible complex refractive indices of secondary organic material produced by photooxidation of the aromatic compounds toluene and m-xylene, Atmos. Chem. Phys., 15, 1435-1446, 10.5194/acp-15-1435-2015, 2015.

Liu, Y., Brito, J., Dorris, M. R., Rivera-Rios, J. C., Seco, R., Bates, K. H., Artaxo, P., Duvoisin, S., Keutsch, F. N., Kim, S., Goldstein, A. H., Guenther, A. B., Manzi, A. O., Souza, R. A. F., Springston, S. R., Watson, T. B., McKinney, K. A., and Martin, S. T.: Isoprene photochemistry over the Amazon rainforest, Proc. Natl. Acad. Sci. U. S. A., 113, 6125-6130, 10.1073/pnas.1524136113, 2016b.

Martin, S. T., Andreae, M. O., Althausen, D., Artaxo, P., Baars, H., Borrmann, S., Chen, Q., Farmer, D. K., Guenther, A., Gunthe, S. S., Jimenez, J. L., Karl, T., Longo, K., Manzi, A., Muller, T., Pauliquevis, T., Petters, M. D., Prenni, A. J., Poschl, U., Rizzo, L. V., Schneider, J., Smith, J. N., Swietlicki, E., Tota, J., Wang, J., Wiedensohler, A., and Zorn, S. R.: An overview of the Amazonian aerosol characterization experiment 2008 (AMAZE-08), Atmos. Chem. Phys., 10, 11415-11438, 10.5194/acp-10-11415-2010, 2010.

Martin, S. T., Artaxo, P., Machado, L. A. T., Manzi, A. O., Souza, R. A. F., Schumacher, C., Wang, J., Andreae, M. O., Barbosa, H. M. J., Fan, J., Fisch, G., Goldstein, A. H., Guenther, A., Jimenez, J. L., Pöschl, U., Silva Dias, M. A., Smith, J. N., and Wendisch, M.: Introduction: Observations and modeling of the green ocean Amazon (GoAmazon2014/5), Atmos. Chem. Phys., 16, 4785-4797, 10.5194/acp-16-4785-2016, 2016.

Massoli, P., Lambe, A. T., Ahern, A. T., Williams, L. R., Ehn, M., Mikkila, J., Canagaratna, M. R., Brune, W. H., Onasch, T. B., Jayne, J. T., Petaja, T., Kulmala, M., Laaksonen, A., Kolb, C. E., Davidovits, P., and Worsnop, D. R.: Relationship between aerosol oxidation level and hygroscopic properties of laboratory generated secondary organic aerosol (SOA) particles, Geophys. Res. Lett., 37, L24801, 10.1029/2010gl045258, 2010.

Mather, J. H., and Voyles, J. W.: The arm climate research facility: A review of structure and capabilities, Bulletin of the American Meteorological Society, 94, 377-392, doi:10.1175/BAMS-D-11-00218.1, 2013.

Moffet, R. C., Henn, T., Laskin, A., and Gilles, M. K.: Automated chemical analysis of internally mixed aerosol particles using X-ray spectromicroscopy at the carbon K-edge, Anal. Chem., 82, 7906-7914, 10.1021/ac1012909, 2010a.

Moffet, R. C., Tivanski, A. V., and Gilles, M. K.: Scanning transmission X-ray microscopy, in: Fundamentals and applications in aerosol spectroscopy, CRC Press, 419-462, 2010b.

Moffet, R. C., Rodel, T. C., Kelly, S. T., Yu, X. Y., Carroll, G. T., Fast, J., Zaveri, R. A., Laskin, A., and Gilles, M. K.: Spectro-microscopic measurements of carbonaceous aerosol aging in central california, Atmos. Chem. Phys., 13, 10445-10459, 10.5194/acp-13-10445-2013, 2013.

Moteki, N., and Kondo, Y.: Effects of mixing state on black carbon measurements by laser-induced incandescence, Aerosol Sci. Technol., 41, 398-417, 10.1080/02786820701199728, 2007.

O'Brien, R. E., Neu, A., Epstein, S. A., MacMillan, A. C., Wang, B. B., Kelly, S. T., Nizkorodov, S. A., Laskin, A., Moffet, R. C., and Gilles, M. K.: Physical properties of ambient and laboratory-generated secondary organic aerosol, Geophys. Res. Lett., 41, 4347-4353, 10.1002/2014gl060219, 2014.

Pajunoja, A., Lambe, A. T., Hakala, J., Rastak, N., Cummings, M. J., Brogan, J. F., Hao, L., Paramonov, M., Hong, J., Prisle, N. L., Malila, J., Romakkaniemi, S., Lehtinen, K. E. J., Laaksonen, A., Kulmala, M., Massoli, P., Onasch, T. B., Donahue, N. M., Riipinen, I., Davidovits, P., Worsnop, D. R., Petäjä, T., and Virtanen, A.: Adsorptive uptake of water by semisolid secondary organic aerosols, Geophys. Res. Lett., 42, 3063-3068, 10.1002/2015gl063142, 2015.

Pajunoja, A., Hu, W., Leong, Y. J., Taylor, N. F., Miettinen, P., Palm, B. B., Mikkonen, S., Collins, D. R., Jimenez, J. L., and Virtanen, A.: Phase state of ambient aerosol linked with water uptake and chemical aging in the southeastern us, Atmos. Chem. Phys., 16, 11163-11176, 10.5194/acp-16-11163-2016, 2016.

Perraud, V., Bruns, E. A., Ezell, M. J., Johnson, S. N., Yu, Y., Alexander, M. L., Zelenyuk, A., Imre, D., Chang, W. L., Dabdub, D., Pankow, J. F., and Finlayson-Pitts, B. J.: Nonequilibrium atmospheric secondary organic aerosol formation and growth, Proc. Natl. Acad. Sci. U. S. A., 109, 2836-2841, 10.1073/pnas.1119909109, 2012.

Petters, M. D., and Kreidenweis, S. M.: A single parameter representation of hygroscopic growth and cloud condensation nucleus activity, Atmos. Chem. Phys., 7, 1961-1971, 10.5194/acp-7-1961-2007, 2007.

Petters, M. D., Carrico, C. M., Kreidenweis, S. M., Prenni, A. J., DeMott, P. J., Collett, J. L., and Moosmuller, H.: Cloud condensation nucleation activity of biomass burning aerosol, J. Geophys. Res. Atmos., 114, D22205, 10.1029/2009jd012353, 2009.

Piens, D. S., Kelly, S. T., Harder, T. H., Petters, M. D., O'Brien, R. E., Wang, B., Teske, K., Dowell, P., Laskin, A., and Gilles, M. K.: Measuring mass-based hygroscopicity of atmospheric particles through in situ imaging, Environ. Sci. Technol., 50, 5172-5180, 10.1021/acs.est.6b00793, 2016.

Pohlker, C., Wiedemann, K. T., Sinha, B., Shiraiwa, M., Gunthe, S. S., Smith, M., Su, H., Artaxo, P., Chen, Q., Cheng, Y. F., Elbert, W., Gilles, M. K., Kilcoyne, A. L. D., Moffet, R. C., Weigand, M., Martin, S. T., Poeschl, U., and Andreae, M. O.: Biogenic potassium salt particles as seeds for secondary organic aerosol in the Amazon, Science, 337, 1075-1078, 10.1126/science.1223264, 2012.

Poschl, U., Martin, S. T., Sinha, B., Chen, Q., Gunthe, S. S., Huffman, J. A., Borrmann, S., Farmer, D. K., Garland, R. M., Helas, G., Jimenez, J. L., King, S. M., Manzi, A., Mikhailov, E., Pauliquevis, T., Petters, M. D., Prenni, A. J., Roldin, P., Rose, D., Schneider, J., Su, H., Zorn, S. R., Artaxo, P., and Andreae, M. O.: Rainforest aerosols as biogenic nuclei of clouds and precipitation in the Amazon, Science, 329, 1513-1516, 10.1126/science.1191056, 2010.

Ramanathan, V., Crutzen, P. J., Kiehl, J. T., and Rosenfeld, D.: Atmosphere - aerosols, climate, and the hydrological cycle, Science, 294, 2119-2124, 10.1126/science.1064034, 2001.

Renbaum-Wolff, L., Grayson, J. W., Bateman, A. P., Kuwata, M., Sellier, M., Murray, B. J., Shilling, J. E., Martin, S. T., and Bertram, A. K.: Viscosity of α-pinene secondary organic material and implications for particle growth and reactivity, Proc. Natl. Acad. Sci. U. S. A., 10.1073/pnas.1219548110, 2013.

Renbaum-Wolff, L., Song, M., Marcolli, C., Zhang, Y., Liu, P. F., Grayson, J. W., Geiger, F. M., Martin, S. T., and Bertram, A. K.: Observations and implications of liquid–liquid phase separation at high relative humidities in secondary organic material produced by α-pinene ozonolysis without inorganic salts, Atmos. Chem. Phys., 16, 7969-7979, 10.5194/acp-16-7969-2016, 2016.

Riipinen, I., Pierce, J. R., Yli-Juuti, T., Nieminen, T., Hakkinen, S., Ehn, M., Junninen, H., Lehtipalo, K., Petaja, T., Slowik, J., Chang, R., Shantz, N. C., Abbatt, J., Leaitch, W. R., Kerminen, V. M., Worsnop, D. R., Pandis, S. N., Donahue, N. M., and Kulmala, M.: Organic condensation: A vital link connecting aerosol formation to cloud condensation nuclei (CCN) concentrations, Atmos. Chem. Phys., 11, 3865-3878, 10.5194/acp-11-3865-2011, 2011.

Riipinen, I., Yli-Juuti, T., Pierce, J. R., Petaja, T., Worsnop, D. R., Kulmala, M., and Donahue, N. M.: The contribution of organics to atmospheric nanoparticle growth, Nature Geosci., 5, 453-458, 10.1038/ngeo1499, 2012.

Saukko, E., Lambe, A. T., Massoli, P., Koop, T., Wright, J. P., Croasdale, D. R., Pedernera, D. A., Onasch, T. B., Laaksonen, A., Davidovits, P., Worsnop, D. R., and Virtanen, A.: Humidity-dependent phase state of SOA particles from biogenic and anthropogenic precursors, Atmos. Chem. Phys., 12, 7517-7529, 10.5194/acp-12-7517-2012, 2012.

Schwarz, J. P., Gao, R. S., Fahey, D. W., Thomson, D. S., Watts, L. A., Wilson, J. C., Reeves, J. M., Darbeheshti, M., Baumgardner, D. G., Kok, G. L., Chung, S. H., Schulz, M., Hendricks, J.,

Lauer, A., Karcher, B., Slowik, J. G., Rosenlof, K. H., Thompson, T. L., Langford, A. O., Loewenstein, M., and Aikin, K. C.: Single-particle measurements of midlatitude black carbon and light-scattering aerosols from the boundary layer to the lower stratosphere, J. Geophys. Res. Atmos., 111, D16207, 10.1029/2006jd007076, 2006.

Shiraiwa, M., and Seinfeld, J. H.: Equilibration timescale of atmospheric secondary organic aerosol partitioning, Geophys. Res. Lett., 39, 10.1029/2012gl054008, 2012.

Song, M., Liu, P. F., Hanna, S. J., Li, Y. J., Martin, S. T., and Bertram, A. K.: Relative humidity-dependent viscosities of isoprene-derived secondary organic material and atmospheric implications for isoprene-dominant forests, Atmos. Chem. Phys., 15, 5145-5159, 10.5194/acp-15-5145-2015, 2015.

Tivanski, A. V., Hopkins, R. J., Tyliszczak, T., and Gilles, M. K.: Oxygenated interface on biomass burn tar balls determined by single particle scanning transmission X-ray microscopy, J. Phys. Chem. A, 111, 5448-5458, 10.1021/jp070155u, 2007.

Tsai, C. J., Pui, D. Y. H., and Liu, B. Y. H.: Capture and rebound of small particles upon impact with solid-surfaces, Aerosol Sci. Technol., 12, 497-507, 10.1080/02786829008959364, 1990.

Ulbrich, I. M., Canagaratna, M. R., Zhang, Q., Worsnop, D. R., and Jimenez, J. L.: Interpretation of organic components from positive matrix factorization of aerosol mass spectrometric data, Atmos. Chem. Phys., 9, 2891-2918, 10.5194/acp-9-2891-2009, 2009.

Vaden, T. D., Imre, D., Beranek, J., Shrivastava, M., and Zelenyuk, A.: Evaporation kinetics and phase of laboratory and ambient secondary organic aerosol, Proc. Natl. Acad. Sci. U. S. A., 108, 2190-2195, 10.1073/pnas.1013391108, 2011.

Virtanen, A., Joutsensaari, J., Koop, T., Kannosto, J., Yli-Pirila, P., Leskinen, J., Makela, J. M., Holopainen, J. K., Poschl, U., Kulmala, M., Worsnop, D. R., and Laaksonen, A.: An amorphous solid state of biogenic secondary organic aerosol particles, Nature, 467, 824-827, 10.1038/nature09455, 2010.

Wang, B., Harder, T. H., Kelly, S. T., Piens, D. S., China, S., Kovarik, L., Keiluweit, M., Arey, B. W., Gilles, M. K., and Laskin, A.: Airborne soil organic particles generated by precipitation, Nature Geosci, 9, 433-437, 10.1038/ngeo2705, 2016.

Zaveri, R. A., Easter, R. C., Shilling, J. E., and Seinfeld, J. H.: Modeling kinetic partitioning of secondary organic aerosol and size distribution dynamics: Representing effects of volatility, phase state, and particle-phase reaction, Atmos. Chem. Phys., 14, 5153-5181, 10.5194/acp-14-5153-2014, 2014.

Zelenyuk, A., Imre, D., Beranek, J., Abramson, E., Wilson, J., and Shrivastava, M.: Synergy between secondary organic aerosols and long-range transport of polycyclic aromatic hydrocarbons, Environ. Sci. Technol., 46, 12459-12466, 10.1021/es302743z, 2012.

Figure Captions

Figure 1. Rebound fraction as a function of apparatus relative humidity during IOP1 (blue) and IOP2 (red), corresponding respectively to the wet and dry seasons in central Amazonia. Panel (a) shows all measurements. Panel (b) shows the subset of data for which the apparatus RH matched the ambient relative humidity (cf. Supplement S3). Panel (c) represents the probability density function of relative humidity at the T3 site during the wet and dry seasons of 2014. Points represent rebound measurements for particles having mobility diameters of 190 nm. Statistics of measurements group by relative humidity are represented in box-whisker format. The horizontal line within a box indicates the median of the points, the horizontal lines at the box boundaries indicate quartiles, and horizontal lines most distant from the box indicate 10% and 90% quantiles. For comparison, the black line shows the rebound curve for particles of secondary organic material produced by photooxidation of an isoprene/α-pinene mixture in the Harvard Environmental Chamber (Bateman et al., 2015).

Figure 2. Probability density function of rebound fraction during (a) IOP1 and (b) IOP2 for categorization by type of air mass and time of day: background conditions (green), Manaus pollution (red), and biomass burning (orange). Solid and dashed lines respectively represent daytime (12:00 to 16:00, local time; 16:00 to 20:00, UTC) and nighttime measurements (23:00 to 04:00, local time; 03:00 to 08:00 UTC). Results are shown for an apparatus RH of 75% and for particles having a mobility diameter of 190 nm. No data sets fit the classification of Manaus pollution during the nighttime of IOP2 (i.e., absence of red dashed line in panel (b)).

Figure 3. Deviation in rebound fraction relative to the average curve for background conditions during (a) IOP1 and (b) IOP2. Red, purple, and green coloring correspond respectively to the RH regions of rebound, transition, and adhesion for the background-average curve. Results are shown for particles having a mobility diameter of 190 nm.

Figure 4. Time series of representative species during two pollution events for IOP1 and IOP2 (left and right sides of figures, respectively). "Total mass concentration" plotted in the figure represents the sum of the AMS and black carbon mass concentrations measured for submicron PM. The PMF mass fractions are expressed in relative terms to one another and necessarily sum to unity. Time on the abscissa is expressed in UTC.

Figure 5. Representative TEM images of (a) adhering and (b) rebounding PM at 95% RH collected between 14:15 and 18:15 (UTC) on September 30, 2014, during IOP2. The rebound fraction during the time period of collection approached 0.3. The arrows in panel (b) highlight the locations of particles having high vertical dimensions and spherical or dome-like morphologies, as expected for solid particles.

Figure 6. Deviation in rebound fraction for categorization by type of air mass and time of day. The box-whisker representation of the 10%, 25%, 50%, 75%, and 90% quantiles of statistics for each RH bin is explained in the caption to Figure 1. Air mass categorization is as for Figure 2. Results are shown for particles having a mobility diameter of 190 nm.

Figure 7. Scatter plot of rebound deviation with the hygroscopicity parameter κ for (a) IOP1 and (b) IOP2. For clarity of presentation, data points are shown for apparatus RH values between 73 and 78%, although the trend applies more broadly. As a guide to the eye, in each panel data are divided into four groups, and medians and quartiles of the groups are plotted as black circles and whiskers, respectively. Different techniques were used to measure κ_G and κ_{CCN}, as described in the main text.

Figure 8. Deviation in rebound fraction for categorization by chemical characteristics. The box-whisker representation of the 10%, 25%, 50%, 75%, and 90% quantiles of rebound fraction is explained in the caption to Figure 1. The chemical characteristics are categorized by the fractional loading of PMF group B as < 0.15 (green), 0.15 to 0.3 (blue), 0.3 to 0.6 (orange), and > 0.6 (red).

Figure 9. Scatter plot of rebound deviation with the fractional loading of PMF group B for (a) IOP1 and (b) IOP2. The data points are colored according to the corresponding hygroscopicity parameter κ. For clarity of presentation, data points are shown for apparatus RH values between 73 and 78%, although the trend applies more broadly. As a guide to the eye, in each panel data are divided into four groups, and medians and quartiles of the groups are plotted as black circles and whiskers, respectively.

Figure 10. Scatter plot of observed compared to predicted rebound deviation for (a) IOP1 and (b) IOP2. Predictions are based on linear combinations of the loadings of the two PMF groups. The linear coefficients used in the prediction were optimized as a function of RH (Table S5). The solid line represents a one-to-one correlation, and the dashed line represents the best linear fit. Coefficients R^2 of determination were

0.65 and 0.72 for the IOP1 and IOP2 datasets, respectively. Points are color-coded by relative humidity.

Figure 11. STXM/NEXAFS analysis of particles collected after rebound from the impaction plate. Samples were collected between 1:00 and 10:00 (UTC) of October 1, 2014. (a) Carbon K-edge spectrum of rebounded particles (red). Lines at 285.4 and 288.5 eV highlight absorption by double bonds (C=C) and carboxylic acids (-COOH), respectively. The line in the region of 286.5 to 286.7 eV can have contributions from ketones, carbonyl-substituted aromatics, and phenolic species. For comparison, spectra are shown for carbonaceous particles collected in other field and laboratory studies: soil organic particles from central USA (Wang et al., 2016), soot from the ambient environment, atmospheric particles collected at a background site in central Amazonia (Pohlker et al., 2012), and three laboratory samples of secondary organic material. Data sources: isoprene-derived SOM produced under HO_2-dominant conditions (O'Brien et al., 2014); isoprene-derived SOM produced under NO-dominant conditions (O'Brien et al., 2014), and toluene-derived SOM produced under NO-dominant conditions (this study). (b) STXM image from which the NEXAFS spectrum of panel (a) was obtained. Coloring is by red for absorption at 285.4 eV (i.e., double bonds). Coloring is by green for other types of functionalities. The pixelation visible in the image corresponds to the STXM spatial resolution during data collection.

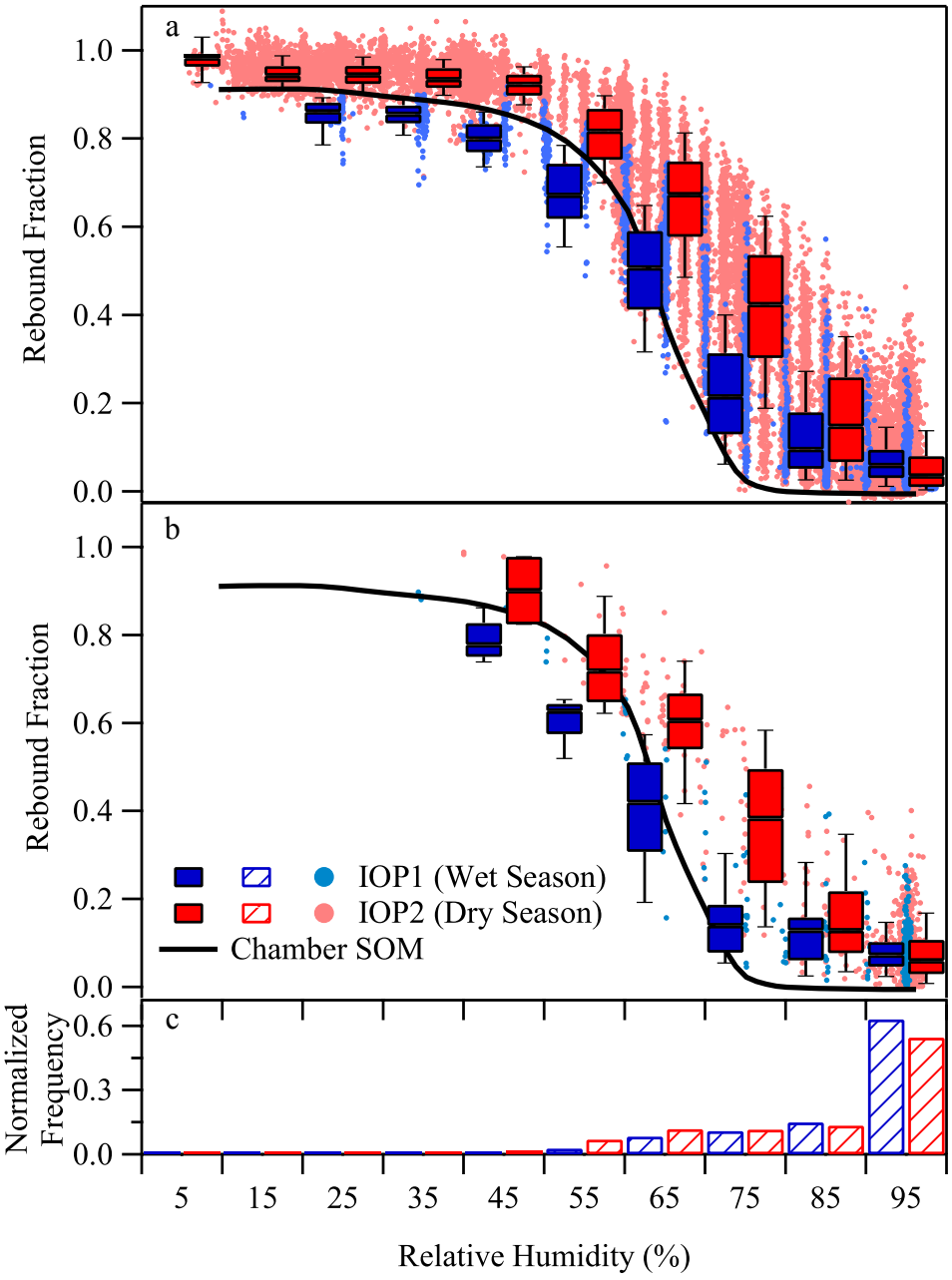
a
b
c
Rebound Fraction
Rebound Fraction
Normalized Frequency
1.0
0.8
0.6
0.4
0.2
0.0
0.6
0.3
0.0
IOP1 (Wet Season)
IOP2 (Dry Season)
Chamber SOM
5
15
25
35
45
55
65
75
85
95
Relative Humidity (%)

Figure 1

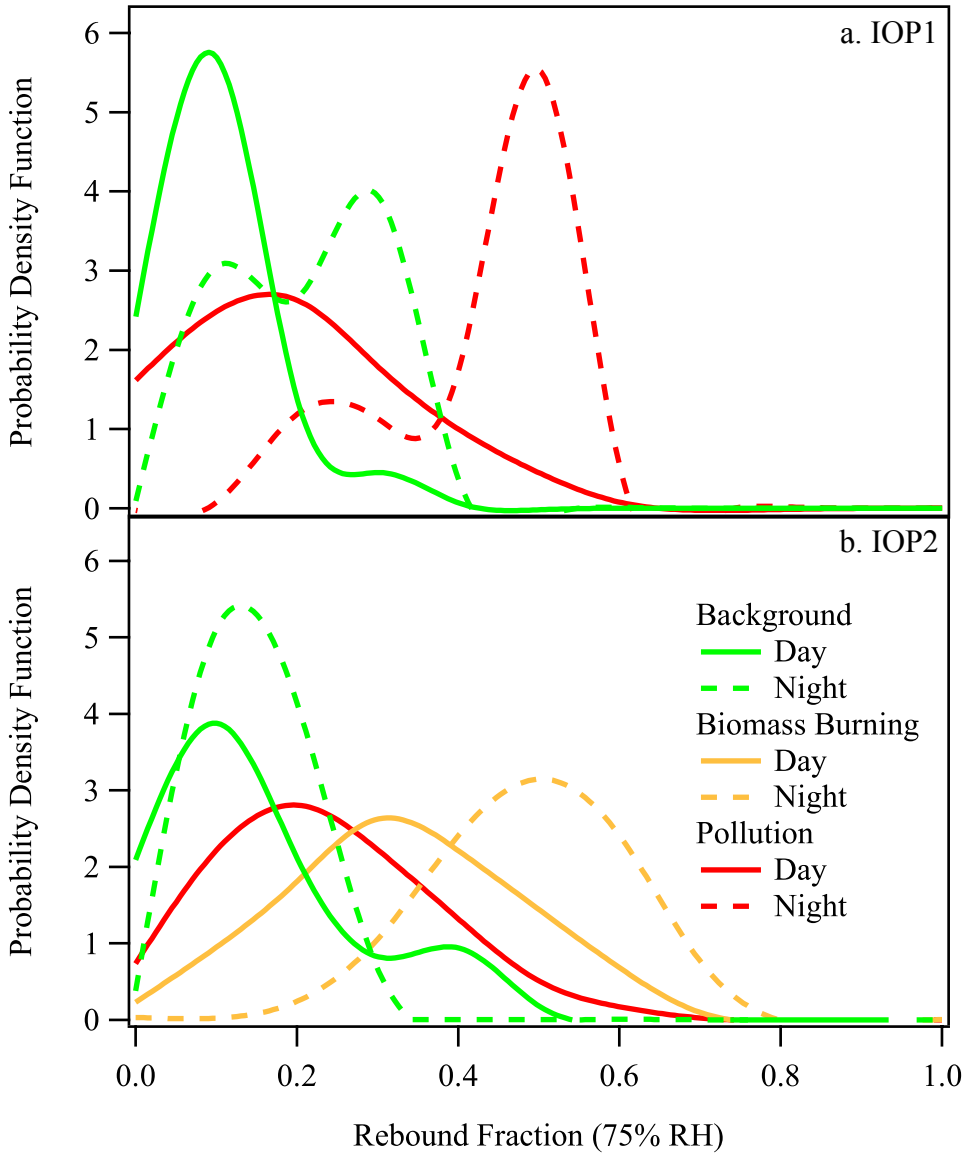
a. IOP1
b. IOP2
Probability Density Function
Probability Density Function
0
1
2
3
4
5
6
0.0
0.2
0.4
0.6
0.8
1.0
Rebound Fraction (75% RH)
Background
Day
Night
Biomass Burning
Day
Night
Pollution
Day
Night

Figure 2

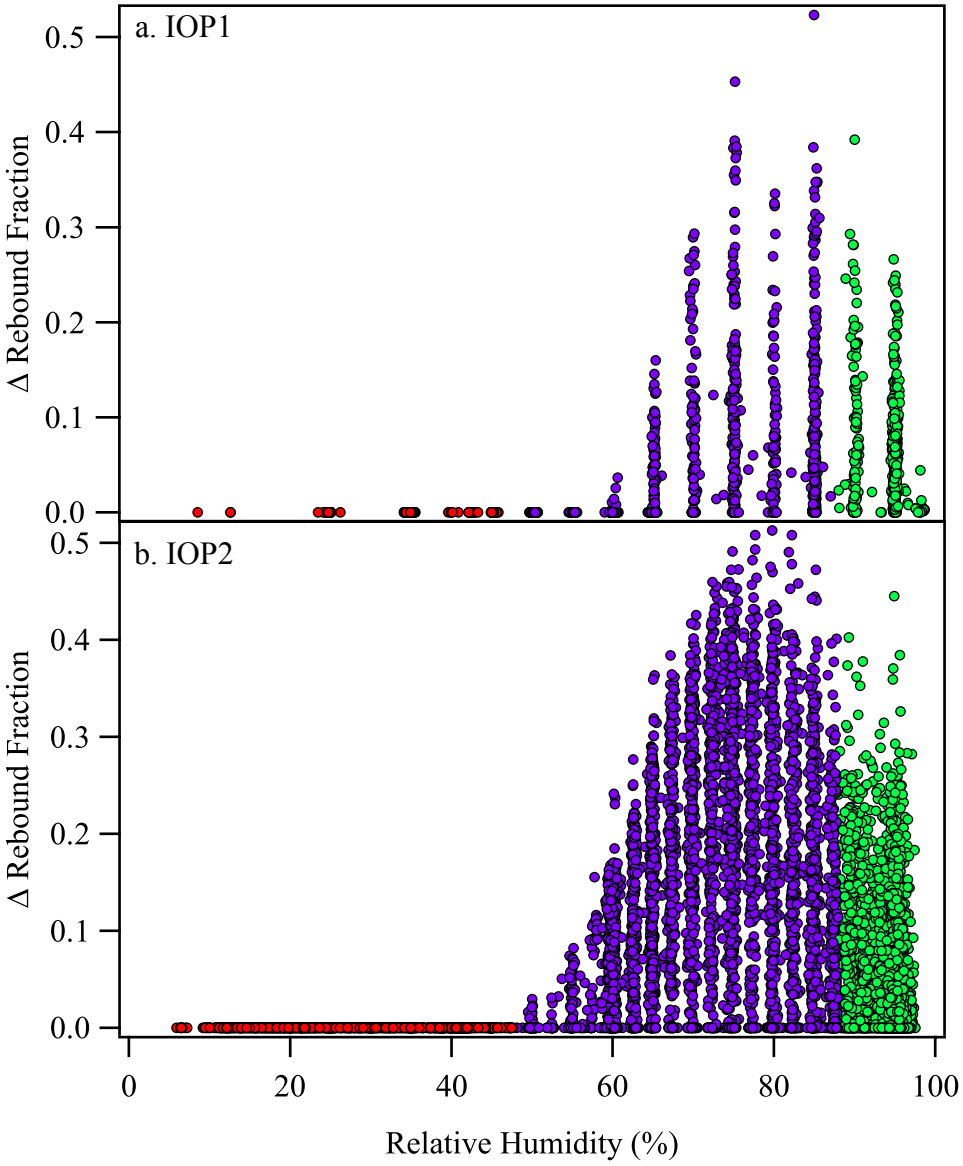
a. IOP1
b. IOP2
Δ Rebound Fraction
Δ Rebound Fraction
0.0
0.1
0.2
0.3
0.4
0.5
0
20
40
60
80
100
Relative Humidity (%)

Figure 3

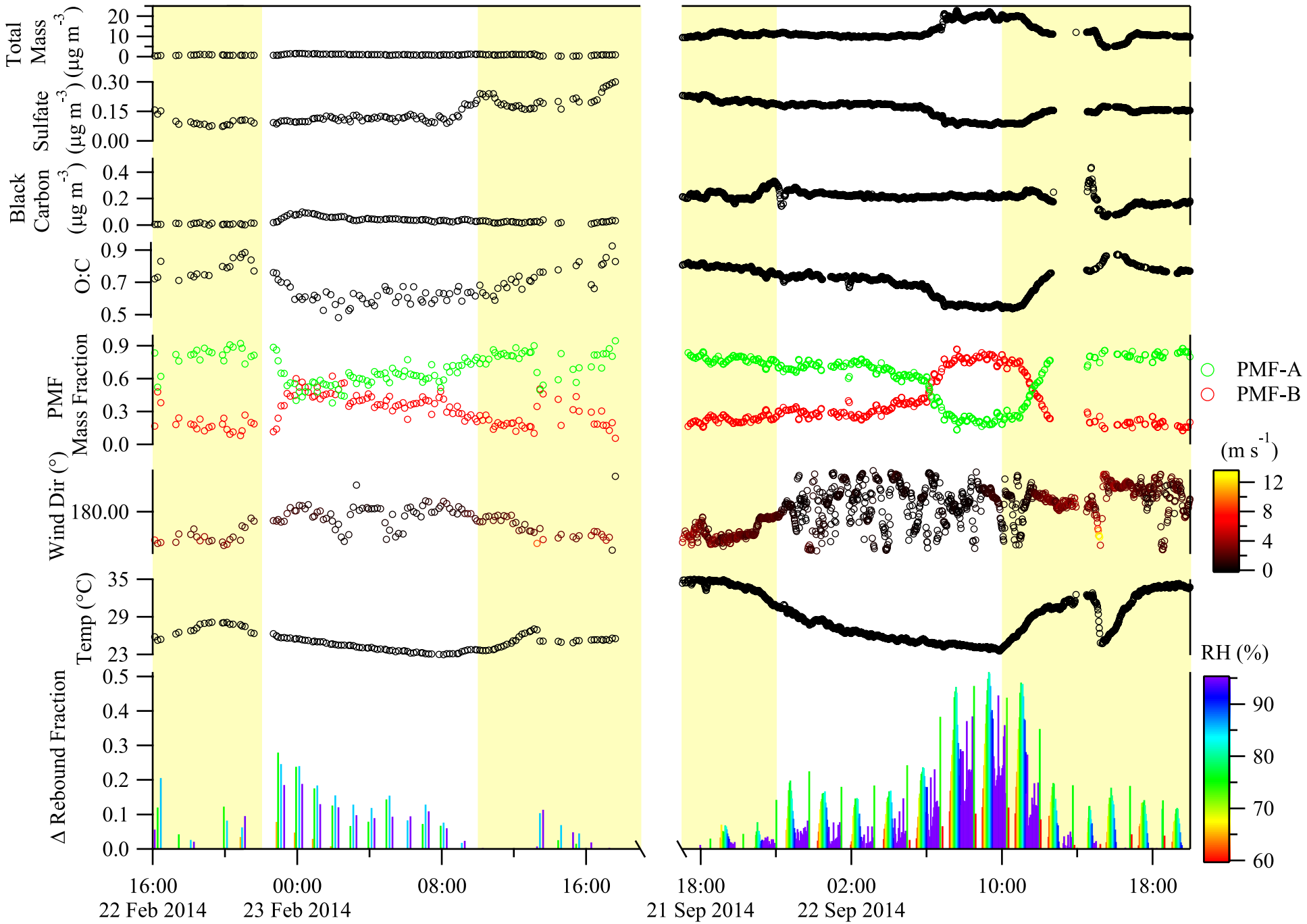
Total Mass (μg m-3)
Sulfate (μg m-3)
Black Carbon (μg m-3)
O:C
PMF Mass Fraction
PMF-A
PMF-B
Wind Dir (°)
(m s-1)
Temp (°C)
RH (%)
Δ Rebound Fraction
16:00
22 Feb 2014
00:00
23 Feb 2014
08:00
16:00
18:00
21 Sep 2014
02:00
22 Sep 2014
10:00
18:00

Figure 4

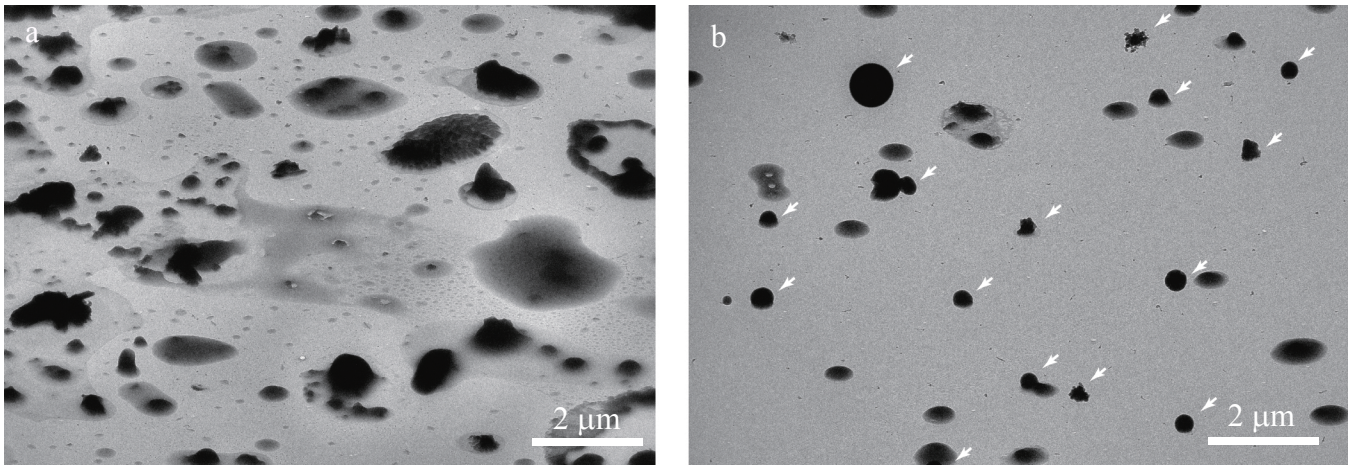

Figure 5

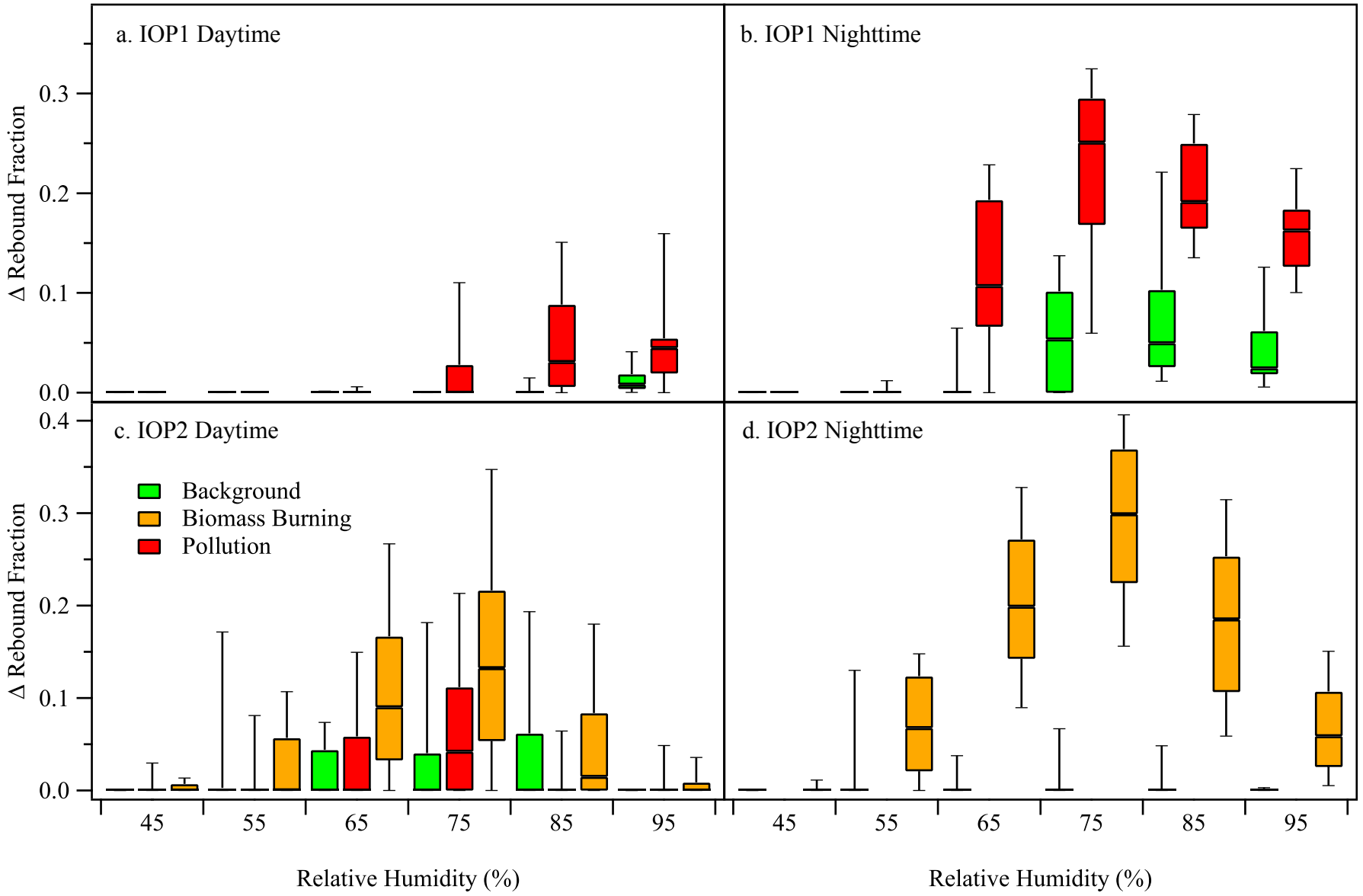
a. IOP1 Daytime
b. IOP1 Nighttime
c. IOP2 Daytime
d. IOP2 Nighttime
Background
Biomass Burning
Pollution
Δ Rebound Fraction
Δ Rebound Fraction
0.0
0.1
0.2
0.3
0.4
45
55
65
75
85
95
Relative Humidity (%)
Relative Humidity (%)

Figure 6

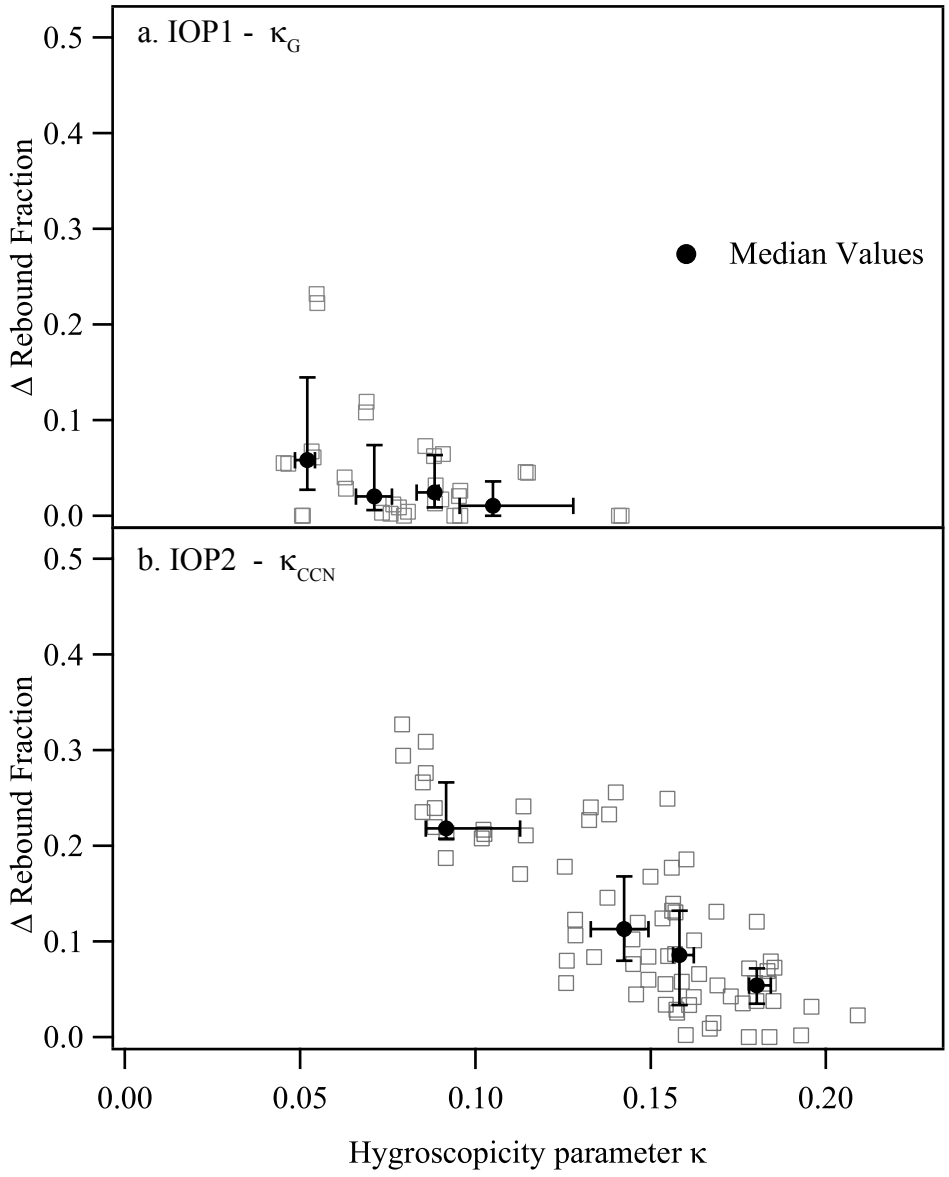
a. IOP1 - κ_G
b. IOP2 - κ_{CCN}
Median Values
Δ Rebound Fraction
Hygroscopicity parameter κ
0.0
0.1
0.2
0.3
0.4
0.5
0.00
0.05
0.10
0.15
0.20

Figure 7

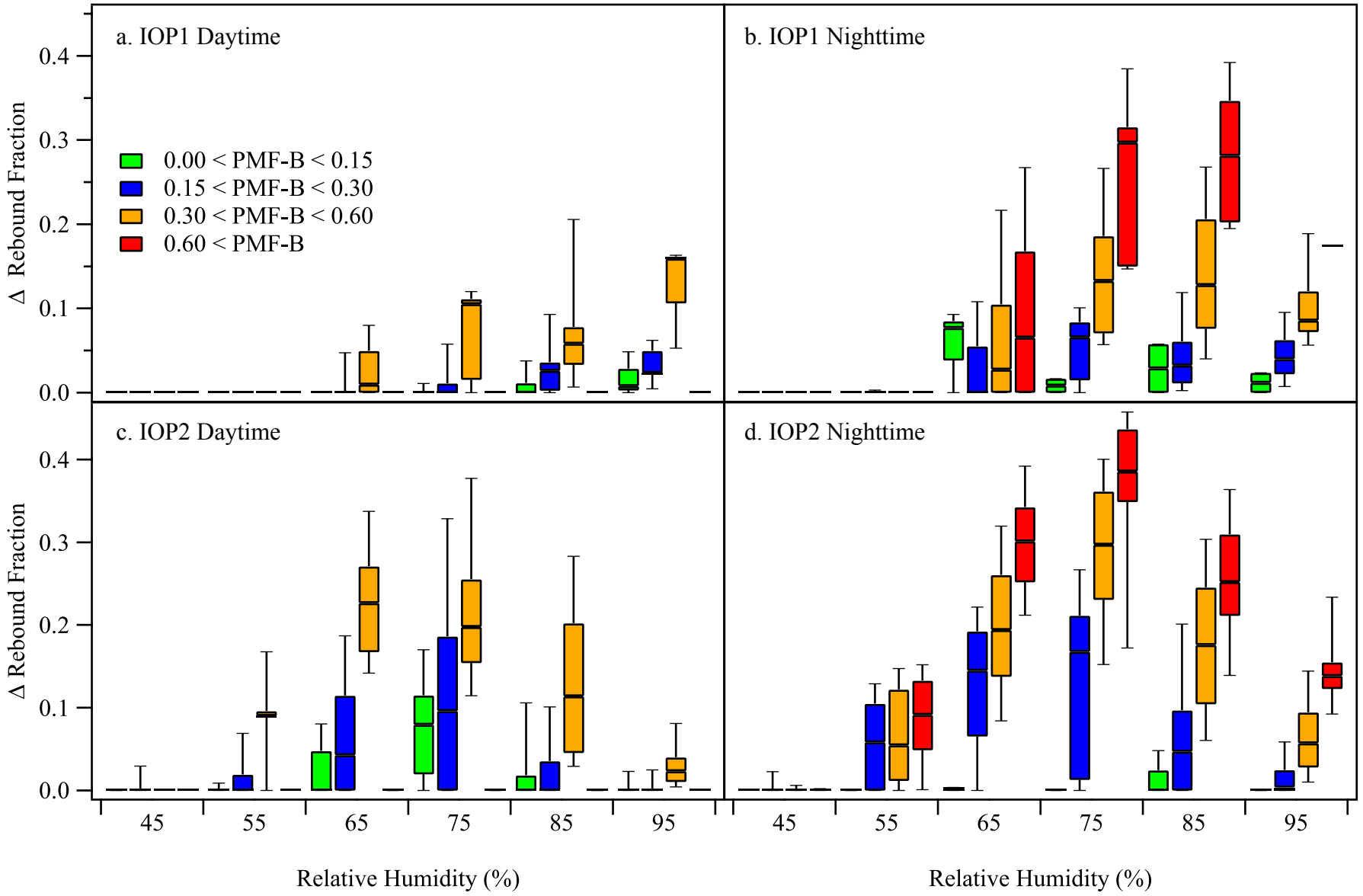
a. IOP1 Daytime
b. IOP1 Nighttime
c. IOP2 Daytime
d. IOP2 Nighttime
0.00 < PMF-B < 0.15
0.15 < PMF-B < 0.30
0.30 < PMF-B < 0.60
0.60 < PMF-B
Δ Rebound Fraction
0.0
0.1
0.2
0.3
0.4
45
55
65
75
85
95
Relative Humidity (%)

Figure 8

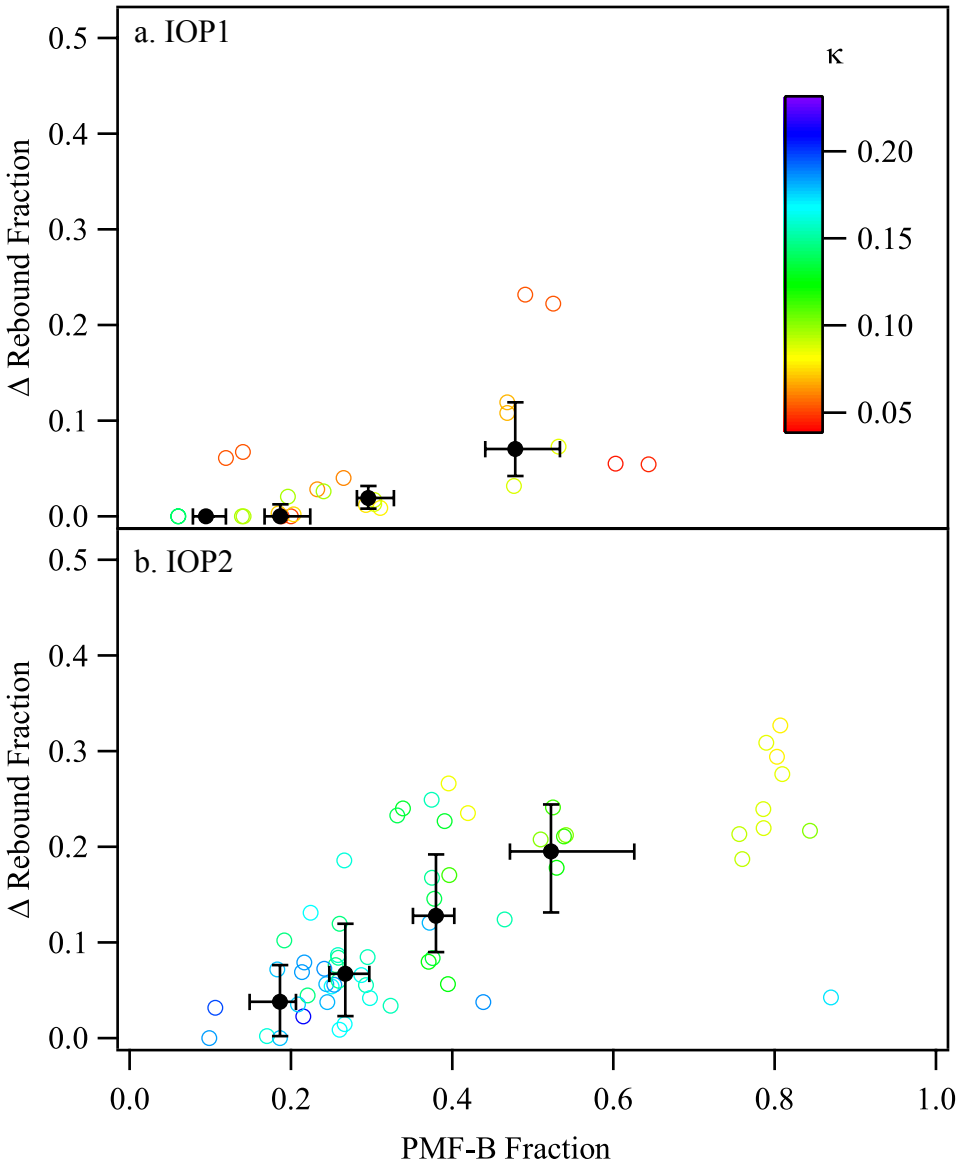
a. IOP1
b. IOP2
κ
0.20
0.15
0.10
0.05
Δ Rebound Fraction
PMF-B Fraction
0.0
0.1
0.2
0.3
0.4
0.5
0.6
0.8
1.0

Figure 9

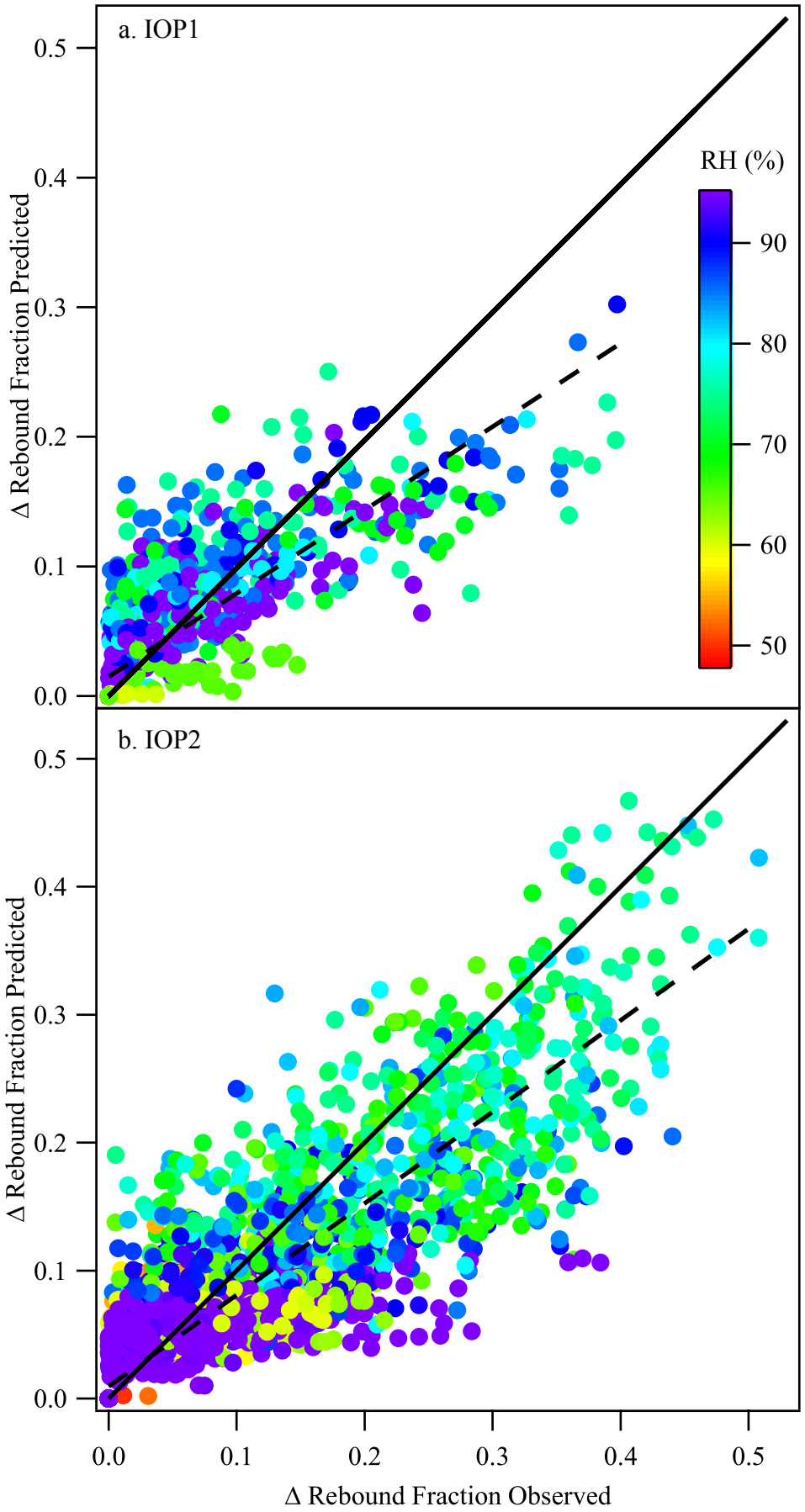
a. IOP1
b. IOP2
RH (%)
90
80
70
60
50
0.0
0.1
0.2
0.3
0.4
0.5
Δ Rebound Fraction Predicted
Δ Rebound Fraction Observed

Figure 10

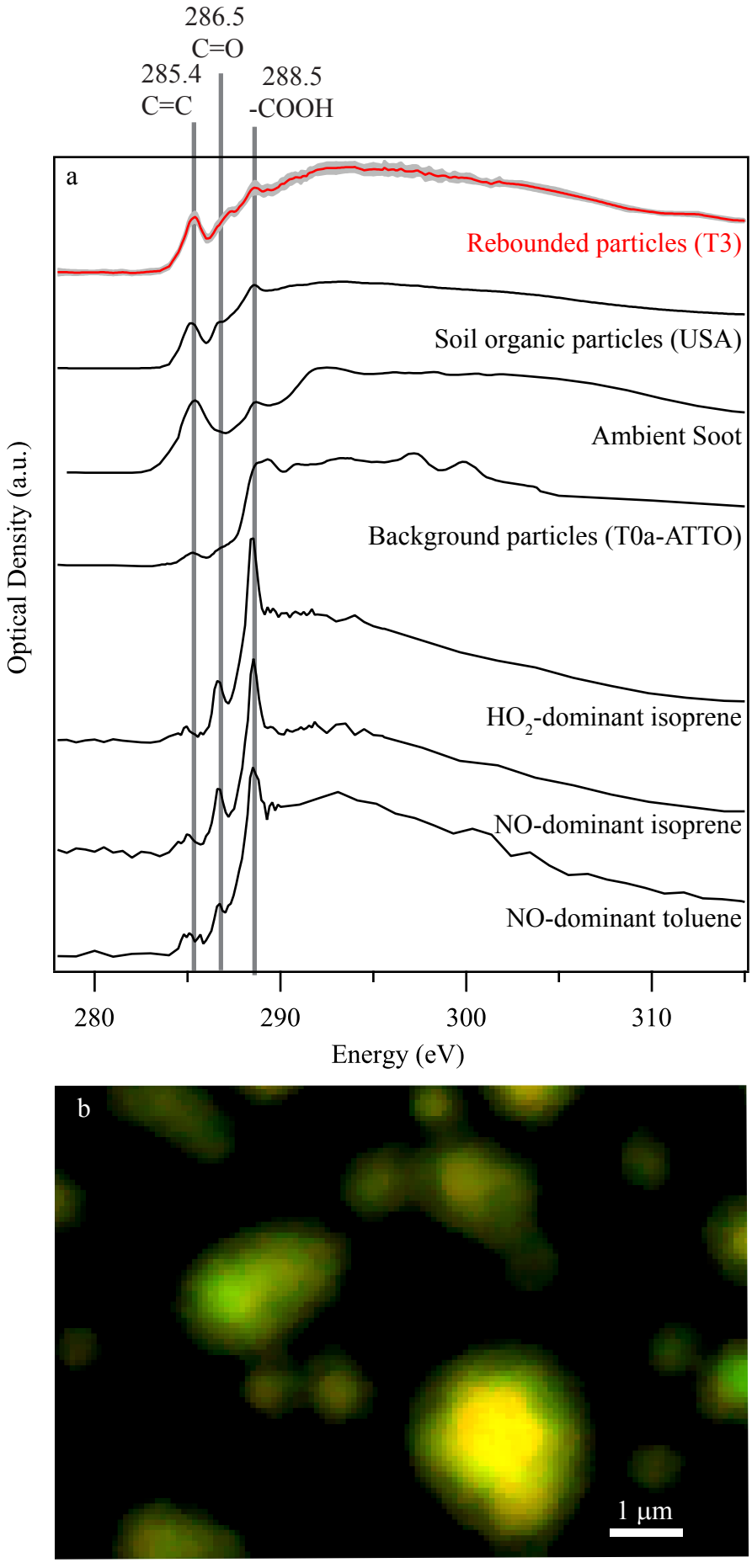
286.5
C=O
285.4
C=C
288.5
-COOH
a
Rebounded particles (T3)
Soil organic particles (USA)
Ambient Soot
Background particles (T0a-ATTO)
HO2-dominant isoprene
NO-dominant isoprene
NO-dominant toluene
Optical Density (a.u.)
280
290
300
310
Energy (eV)
b
1 µm

Figure 11

Supplement

S1. Impactor protocols

A rebound curve representing *f*(RH) constituted an individual data set, where *f* is the rebound fraction of Equation 1. The DMA setting for electric mobility was held constant, the RH in the humidification unit was scanned stepwise, and *f* was continuously recorded. During the course of measurements, rebound curves were collected by several protocols. During IOP1, these protocols included: (1) constant RH while increasing the mobility diameter in variable steps every 3 min from 50 to 190 nm, resulting in a full sweep in 30 min; (2) constant RH while shifting mobility diameter among 120, 150, and 190 nm every 16 min; and (3) fixed mobility diameter at 190 nm while increasing the RH stepwise every 5 to 10 min. For each of these three protocols, 8 to 11 RH levels were probed to produce a rebound curve. The data in the main text correspond to the third protocol, and a rebound curve was collected in 40 to 90 min. Some of the supplementary figures represent data collected with the other two protocols. For IOP2, improved computer control over the apparatus allowed more efficient protocols to be used: (1) constant RH while shifting mobility diameters among 150, 190, and 240 nm every 3 to 5 min and (2) fixed mobility diameter at 190 nm while increasing RH stepwise every 3 to 5 min. RH levels were also controlled at a finer scale, and a rebound curve consisted of 20 RH settings. The data in the main text correspond to the second protocol, and a rebound curve was collected in 30 to 60 min.

S2. Microscopy Description

An X-ray beam obtained at soft wavelengths from the synchrotron light source was used to probe chemical bonding of specific elements of interest within individual particles. Carbon and oxygen K-edge NEXAFS spectra were acquired in this study. Mixing state and chemical bonding of elements within individual particles at a size resolution of 35 nm were identified by

analyzing the recorded spectra. A set ("stack") of STXM images was obtained by raster scanning the sample at fixed photon energy and recording intensities of the transmitted X-rays at each pixel. The spatially resolved NEXAFS spectra were retrieved for the specific areas of interest from the recorded STXM stacks.

S3. Determining rebound fraction at ambient RH

The ambient RH was monitored continuously during the GoAmazon2014/5 campaign. Data were obtained at one-minute intervals by the ARM Mobile Facility One (AMF-1). Rebound fractions were associated with ambient RH values which matched the apparatus (inlet) RH bins within 15 min of measurement. Nine bins were used for IOP1 with RH values of 0, 58, 63, 68, 73, 78, 83, 88, 93, and 100%. Twenty-two bins were used for IOP2 with RH values of 0, 35, 40, 45, 50, 55, 60, 62.5, 65, 67.5, 70, 72.5, 75, 77.5, 80, 82.5, 85, 87.5, 90, 92.5, 97.5, and 100%.

The results of the binning method are shown in Figure S4. The rebound fraction is displayed versus the apparatus (inlet) relative humidity for (a) IOP1 and (d) IOP2 and versus the ambient relative humidity for (b) IOP1 and (e) IOP2. An evaluation of the RH binning procedure can be seen in (c) IOP1 and (f) IOP2, which display the apparatus RH versus the ambient RH. The coefficients R^2 of determination for the linear fits in (c) and (f) are listed in Table S6. The range seen in ambient values obtained from each inlet RH bin arises from the 15-min intervals used to match apparatus RH and ambient RH values. The multiple values for apparatus (inlet) RH obtained from the lowest ambient RH values are due to the large bin used, i.e., 0 to 58 % RH and 0 to 35 % RH for IOP1 and IOP2, respectively.

S4. Air-Mass Classification

Two separate air mass classification schemes were used in conjunction to determine the predominant conditions at the T3 site. The first classification scheme was used primarily to

identify time periods when the T3 site was influenced by anthropogenic pollution from Manaus (Cirino et al., in preparation). In the cited study, particle number and CO concentrations were used to indicate the presence of Manaus plume. Herein, the 25% and 75% quantiles were used to define the thresholds for the T3 site according to the bounds listed in Table S7. Background conditions were indicated when concentrations were below the thresholds listed in Table S7. Observations at a remote forest site T0a were used to establish the thresholds (Thalman et al., in preparation). The established thresholds were different depending on the dry or wet season. Biomass burning conditions were determined by the threshold number of particles and the number fraction of particles below 70 nm. The threshold value for the number fraction is indicated in Table S7. The periods not resolved (i.e., "unclassified") includes cases of (i) unavailable from the monitoring instruments (e.g., maintenance or repair) and (ii) all simultaneous criteria needed for positive classification were not met. The number and fraction of data points classified into the four categories are listed in Table S8.

S5. Deviations relative to background conditions calculation

The deviations relative to background conditions represent the contribution to the rebound fraction above the background-average rebound response curve. The reference curve is based on data sets for which the rebound fraction was less than 0.05 at an apparatus RH of 80%. The reference curves for IOP1 and IOP2 are plotted in the left and right panels of Figure S5, respectively. In each panel, the black line is the reference curve, and the red lines represent upper and lower bounds, respectively, based on one-sigma error propagation of the CPC measurements. The green points are within the envelope of the reference curves determined for IOP1 and IOP2.

For all data points, the deviation Δf relative to the reference curve was calculated as follows:

$$\begin{aligned} &\text{For } f(RH) < f_{\text{upper,reference}}, \Delta f(RH) = f(RH) - f_{\text{upper,reference}}(RH). \\ &\text{Otherwise, } \Delta f(RH) = 0. \end{aligned} \quad \text{(S1)}$$

The spread in rebound fractions for RH < 50% is investigated in Figure S6a. The rebound fractions from a variety of materials are plotted as a function of RH, including chamber PM, Amazonia PM measured during 2013, and particles of sucrose, citric acid, and ammonium sulfate. The reference curves from IOP1 and IOP2 are plotted for comparison. The measured rebound fractions ranged from 0.8 to 1.1 for the investigated materials. Even though there are differences in physical state (e.g., crystalline, amphorous solid, and so on) for the investigated materials, there is no systematic trend for RH < 50% that can be associated with the known physical states and thus applied as a rubric to the scatter observed from the field data. The large spread in measured rebound fractions at RH < 50% observed during IOP1 and IOP2 cannot then be used to distinguish a potential distribution of particle viscosities.

The spread in measured rebound fractions for RH > 50% is investigated in Figure S6b. The same set of test compounds are used as in Figure S6a. The rebound response curves of the organic test materials exhibit shifts at RH values according to their relative hygroscopicity. Particle rebound greater in excess of the reference curve (i.e., rebound deviation) can therefore be used as a proxy for semisolidity for RH > 50%.

S6. AMS PMF Factors

Six positive matrix factorization (PMF) factors explained the variance in the AMS datasets during IOP1 and IOP2. Labeled as factors "1" through "6", these factors traditionally have been associated with the processes/classes of (1) IEPOX-derived secondary organic species (IEPOX-SOA), (2) more-oxidized (i.e., "aged") secondary organic species (MO-OOA), (3) less-

oxidized (i.e., "fresher") secondary organic species (LO-OOA), (4) more-oxidized biomass burning compounds (MO-BBOA), (5) less-oxidized biomass burning compounds (LO-BBOA) for IOP2 and a factor currently hypothesized to be representative of organic material derived from aromatic compounds for IOP1, and (6) hydrocarbon-like organic compounds from unburned primary emissions released by fuel combustion (HOA) (de Sá et al., 2016). The PMF factors obtained for each season were for the most part similar, except for factor 5. For IOP2, factor 5 reflected the increase in local and regional biomass burning in the dry season, which allowed for a separation of a second BBOA factor, while for IOP1 it reflected the influence of urban pollution reaching T3 in the absence of extensive biomass burning (de Sá et al., 2016).

In the present study, the loadings of PMF factors 1, 2 and 3, and PMF factors 4, 5, and 6 were separately lumped. The respective groupings are referred to as PMF group A and PMF group B. PMF group A represents the influence of background processes while PMF group B represents the influences of urban pollution and biomass burning processes.

S7. Probability density function of rebound deviation segregated by air mass type

The distribution of rebound deviations relative to background conditions for each classification and IOP are listed in Table S2. Deviations relative to background conditions of greater than +0.1 represented 17% of the total observations during IOP1. Deviations of greater than +0.1 represented 35% of the total observations for IOP2. The increase in the frequency of large deviations relative to background conditions during IOP2 compared to IOP1 is explained by the influence of biomass burning.

S8. κ_G Determination for subsaturated conditions

The analysis for determing κ_G was published previously (Bateman et al., 2016). A brief description is provided herein. The transmission functions $\Omega_{uncoated}$ and Ω_{coated} for the uncoated and coated arms, respectively, were calculated as follows:

$$\Omega_{\text{uncoated}} = \frac{N_{\text{i}}}{N_{\text{iii}}},\ \Omega_{\text{coated}} = \frac{N_{\text{ii}}}{N_{\text{iii}}} \tag{S2}$$

from transmitted particle number concentrations N measured by the three condensation particle counters. The sigmoid function representing the transmission function was used to fit the setpoint mobility diameter d_m^* and a width parameter δ.

$$\Omega(d_m) = \frac{1}{1+\exp\left(\left(d_m - d_m^*\right)/\delta\right)} \tag{S3}$$

The fit value of d_m^* was converted to a setpoint aerodynamic diameter d_a^* according to:

$$d_a = \left(\frac{\rho_p}{\rho_0}\frac{C_c(d_m)}{C_c(d_a)}\right)^{1/2} d_m \tag{S4}$$

This equation is for a limiting assumption of nonporous spherical particles having +1 charge (Kelly and McMurry, 1992). Terms include the particle material density ρ_p, a reference material density ρ_0 (1000 kg m^{-3}), and the Cunningham slip correction factors $C_c(d_m)$ and $C_c(d_a)$.

Of key interest for determing κ_G, the material density $\rho_{p,i}$ of the different data sets i depended on relative humidity. The density was assumed to follow a volume mixing rule between $\rho_{p,\text{dry}}$ of the organic material and $\rho_{p,\text{water}}$ of water (Brechtel and Kreidenweis, 2000). The fractional particle water volume was derived by assuming the following relationship:

$$G = \left[1+\left(\frac{\text{RH}/100}{\text{1-RH}/100}\right)\kappa\right]^{1/3} \tag{S5}$$

In this equation, G is the diameter-based hygroscopic growth factor, RH is relative humidity, and κ is the hygroscopicity parameter. Values of $\rho_{p,\mathrm{dry}}$ and κ, as needed to estimate $\rho_{p,i}$ of each experiment, were obtained by optimization of four datasets. The minimized quantity was $\sum_i \left(d^*_{a,i} - d^*_{a,0}\right)^2$ for each dataset for which $d^*_{a,0}$ = 84.9 nm. For each i, $d^*_{a,i}$ was obtained using Equation S4 with parameter values of $d^*_{m,i}$ and $\rho_{p,i}(\rho_{p,\mathrm{dry}},\kappa)$ obtained by the volume mixing rule. Values of $\rho_{p,\mathrm{dry}}$ and κ were taken as constant within each RH-dependent dataset. The values of κ were then averaged over the four successive datasets to obtain the values used in the Figure 7.

The measured κ_G during IOP1 can be compared with literature values from hygroscopic tandem differential mobility analyzer (H-TDMA) instruments. The results from several studies in Amazonia are compiled in Table S4. There are several important distinctions to note between the H-TDMA measurements and the measurements of κ_G by the impactor apparatus. Particle rebound ceases for $G > 1.10 \pm 0.02$ corresponding to a κ_G of 0.06 at 90% RH. The impactor apparatus while being operated at 90% RH is then able to distinguish particles with κ_G of less than 0.06 from those with κ_G greater than 0.06. The measured value is thus a lower limit of the actual value because any particle having $\kappa_G > 0.06$ ($f = 0$) cannot be distinguished from particles of greater κ_G. Particles of differing κ_G can be distinguished as a function of RH as in the impactor apparatus. Therefore, in the analysis κ_G values are evaluated for datasets obtained at multiple RH values and averaged to obtain a global κ_G.

S9. Modeled compared to measured rebound deviation

Rebound deviation was predicted according to the following equation:

$$\Delta f_{predicted}(\mathrm{RH}) = \mathrm{PMF\text{-}A} \cdot x_1 + \mathrm{PMF\text{-}B} \cdot x_2 \qquad \text{(S6)}$$

where PMF-A and PMF-B are the fractional loadings of PMF groups A and x_1 and x_2 are linear coefficients. The coefficients were obtained by optimization of each dataset as a function of RH.

The minimized quantity was $\sum_i \left(\Delta f(\mathrm{RH})_{predicted,i} - \Delta f(\mathrm{RH})_{measured} \right)^2$ for each season and RH range.

The RH ranges are listed in Table S5 along with the optimized coefficients.

Table S1. Percent of data points when grouped into steps of 0.05 rebound fraction. "All Data" refers to measurements collected at all apparatus RH values. "Ambient RH" refers to measurements collected when the apparatus RH matched the ambient RH value (cf. Supplement S3). Cumulative values are represented in parentheses.

Rebound Deviation	All Data		Ambient RH	
	IOP1	IOP2	IOP1	IOP2
< 0.05	71.3% (71.3%)	50.4% (33.9%)	44.9% (44.9%)	53.8% (53.8%)
0.05 – 0.10	12.2% (83.5%)	14.8% (65.2%)	34.7% (79.5%)	22.6% (76.4%)
0.10 – 0.20	11.2% (94.7%)	18.4% (83.6%)	16.5% (96.0%)	17.6% (94.0%)
0.20 – 0.30	4.1% (98.8%)	9.8% (93.4%)	3.3% (99.3%)	4.7% (98.7%)
0.30 – 0.40	1.1% (99.9%)	5.5% (98.9%)	0.7% (100%)	1.3% (100.0%)
> 0.40	<0.1% (100%)	1.1% (100%)	0.0 % (100%)	0.0% (100%)

Table S2. Percent of all data points when grouped into steps of 0.05 rebound fraction according to type of air mass. Cumulative values are represented in parentheses.

	Background Conditions		Manaus Pollution		Biomass Burning		Unclassified	
Rebound Deviation	**IOP1**	**IOP2**	**IOP1**	**IOP2**	**IOP1**	**IOP2**	**IOP1**	**IOP2**
< 0.05	81.3% (81.3%)	80.6% (80.6%)	51.7% (51.7%)	66.8% (66.8%)	-	42.8% (42.8%)	65.4% (65.4%)	57.9% (57.9%)
0.05 – 0.10	7.9% (89.2%)	9.0% (89.6%)	14.0% (65.7%)	14.9% (81.7%)	-	15.6% (58.4%)	18.8% (84.2%)	14.9% (72.8%)
0.10 – 0.20	8.6% (97.8%)	7.0% (96.6%)	17.2% (82.9%)	12.9% (94.6%)	-	21.2% (79.6%)	12.6% (96.8%)	16.0% (88.8%)
0.20 – 0.30	1.5% (99.3%)	3.1% (99.7%)	12.5% (95.4%)	4.6% (99.2%)	-	11.9% (91.5%)	2.8% (99.6%)	6.6% (95.4%)
0.30 – 0.40	0.7% (100%)	0.3% (100%)	4.3% (99.7%)	0.7% (99.9%)	-	7.1% (98.6%)	0.4% (100%)	4.0% (99.4%)
> 0.40	0.0% (100%)	0.0% (100%)	0.3% (100%)	0.1% (100%)	-	1.5% (100%)	0.0% 100%)	0.7% (100%)

Table S3. The average O:C ratios of the various air mass classifications. $O:C_{All}$ represents an average over all times. $O:C_{Nighttime}$ represents an average over 23:00 to 04:00 (local time) (03:00 to 08:00 UTC). $O:C_{Daytime}$ represents an average over 12:00 to 16:00 (local time) (16:00 to 20:00 UTC).

	Background Conditions		Manaus Pollution		Biomass Burning	
	IOP1	IOP2	IOP1	IOP2	IOP1	IOP2
$O:C_{All}$	0.79 ± 0.12	0.81 ± 0.07	0.72 ± 0.12	0.80 ± 0.06	-	0.73 ± 0.08
$O:C_{Nighttime}$	0.73 ± 0.10	0.78 ± 0.06	0.61 ± 0.05	-	-	0.69 ± 0.07
$O:C_{Daytime}$	0.89 ± 0.12	0.87 ± 0.05	0.81 ± 0.09	0.83 ± 0.06	-	0.82 ± 0.05

Table S4. Comparison of κ_G values of hydrophobic and hygroscopic fraction of particles using H-TDMA measurements (literature) with the values obtained from the impactor apparatus (current study). Population fractions correspond to dry diameters of 190 nm for IOP1 and both 190 and 240 nm for IOP2. Growth factor data from IOP1 and the study of 2013 reported in Bateman et al. (2016) are associated with dry particle diameters of 50 to 70 nm.

[see table next page]

Particle Population Distribution	Wet Season				Transition Season				Dry Season		
	IOP1 – All Data	2013	†LBA – SMOCC -2002	†CLAIRE – 98	†LBA – SMOCC - 2002	†CLAIRE – 2001 Clean	†CLAIRE – 2001 Recent BB	†CLAIRE – 2001 Aged BB	IOP2 – All Data	2013	†LBA – SMOCC-2002
Hydrophobic Particles											
Frequency of Occurrence	56.5%	-	89 - 92 %	14 - 11 %	96 - 97 %	26% - 49 %	58 - 76%	21 - 79%	39.4%	-	99 - 99%
Number Fraction (when present)	0.095 ± 0.060	-	0.40 - 0.34 ±0.21	0.31 - 0.24 ± 0.19	0.62 - 0.42 ±0.26	0.14 - 0.28 ±0.11	0.19 - 0.23 ±0.12	0.18 -0.34 ±0.17	0.100 ± 0.069	-	0.84 - 0.69 ±0.29
κ	0.041	-	0.040 -0.047	0.003 - 0.010*	0.036 - 0.043	0.018 - 0.058*	0.045 - 0.045*	0.049 - 0.058*	-	-	0.037 -0.044
Hygroscopic Particles											
Frequency of Occurrence	100%	-	99 - 100 %	95 - 97 %	86 - 96 %	100 - 100%	100%	100 - 100%	100%	-	51 - 66 %
Number Fraction (when present)	0.937 ± 0.066	-	0.66 - 0.69 ±0.23	0.94 - 0.97 ± 0.15	0.47 - 0.62 ±0.24	0.96 - 0.86 ± 0.17	0.88 - 0.83 ±0.14	0.96 - 0.73 ±0.21	0.958 ± 0.067	-	0.32 - 0.48 ±0.22
κ	0.090	-	0.124 - 0.146	0.111 -0.144*	0.113 -0.123	0.122 -0.150*	0.150 - 0.168*	0.139 - 0.162*	-	-	0.111 - 0.113
κ, both modes‡	0.09	0.053	0.124-0.128	0.096-0.115‡	0.106-0.112	0.108-0.118‡	0.117-0.122‡	0.116-0.116‡	-	0.063	0.079-0.094

*****Values of κ were not reported in the original manuscript and have been calculated according to Equation S5 using the reported G values.
†Range of values is for particles of 165 nm and 265 nm
‡Average values of κ for both modes are calculated assuming volume additivity.

Table S5. The optimized coefficients used to predict rebound deviation (Equation S6).

IOP1	PMF Group A	PMF Group B
	x_1	x_2
48 – 53% RH	0.00	0.00
53 – 63% RH	0.00	0.00
63 – 68% RH	0.00	0.06
68 – 73% RH	0.00	0.27
73 – 78% RH	0.00	0.33
78 – 83% RH	0.00	0.30
83 – 88% RH	0.00	0.33
88 – 93% RH	0.00	0.32
> 93% RH	0.00	0.25

IOP2	PMF Group A	PMF Group B
	x_1	x_2
48 – 53% RH	0.00	0.00
53 – 63% RH	0.01	0.16
63 – 68% RH	0.03	0.39
68 – 73% RH	0.04	0.51
73 – 78% RH	0.04	0.55
78 – 83% RH	0.00	0.51
83 – 88% RH	0.00	0.37
88 – 93% RH	0.00	0.24
> 93% RH	0.00	0.14

Table S6. Statistics on the binning method used to predict the rebound fraction at ambient RH from the measurements of rebound fraction at specific apparatus RH values (cf. Figure S4).

	Apparatus RH Bin Method	
	IOP1	IOP2
Number of Matched Data Points	308 (8%)	3055 (11%)
Coefficient R^2 of Determination Between Apparatus and Ambient RH	0.94	0.95

Table S7. Parameters and bounds used to classify the air masses passing over the T3 site. Classifications include background, pollution, or biomass burning. Time periods that did not fit these bounds are labeled unclassified. The parameters included the particle number concentrations (CN), ratio of the latter to ΔCO (where ΔCO was the difference in CO measured at the T3 site and the T2 site to account for dilution), the concentration of gas-phase NO_y, and the fraction (CN_{frac}) of particles smaller 70 nm.

Classification	Wet Season (IOP1)	Dry Season (IOP2)
Background	40 cm^{-3} ppbv > CN/ΔCO CN < 500 cm^{-3} CO < 140 ppbv NO_y < 0.9 ppbv	40 cm^{-3} ppbv > CN/ΔCO CN < 1500 cm^{-3} NO_y < 1.5 ppbv
Pollution	40 < CN/ΔCO <130 cm^{-3} ppbv	40 < CN/ΔCO <130 cm^{-3} ppbv
Biomass Burning	CN > 500 cm^{-3} CN_{frac} < 0.45	CN>1500 cm^{-3} CN_{frac} < 0.45

Table S8. The frequency of occurrence for each classification along with the total number of data points in that classification.

	Background Conditions		Manaus Pollution		Biomass Burning		Unclassified	
	IOP1	IOP2	IOP1	IOP2	IOP1	IOP2	IOP1	IOP2
Frequency	17%	10%	24%	11%	-	71%	58%	8%
Number of Points	278	911	400	955	-	6377	972	717

Table S9. Time series of data.

[See electronic attachment to the PDF file]

Figure Captions

Figure S1. Rebound fraction for categorization by type of air mass and time of day. The box-whisker representation of the 10%, 25%, 50%, 75%, and 90% quantiles of statistics for each RH bin is explained in the caption to Figure 1. Air mass categorization is as for Figure 2. Results are shown for particles having a mobility diameter of 190 nm.

Figure S2. Scatter plot of rebound deviation with meteorological measurements at the T3 site. Correlations with ambient temperature, wind direction, and wind speed are shown for (a) IOP1 daytime, (b) IOP1 nighttime, (c) IOP2 daytime, and (d) IOP2 nighttime. Median values for four bins having equal numbers of data points are indicated by black circles. Whiskers represent quartile values. Relative humidity is variable throughout the data points in the panels, corresponding to all data points shown in Figure 1a.

Figure S3. Scatter plot of rebound deviation with auxiliary particle measurements at the T3 site. Correlations with submicron particle mass concentration, black carbon concentration, and sulfate concentration are shown for (a) IOP1 daytime, (b) IOP1 nighttime, (c) IOP2 daytime, and (d) IOP2 nighttime. Median values for four bins having equal numbers of data points are indicated by black circles. Whiskers represent quartile values.

Figure S4. Rebound fraction and relative humidity after co-binning. The top and bottom panels are associated with IOP1 and IOP2, respectively. The first column (panels a and d) displays the rebound fraction as a function of the apparatus (inlet) relative humidity. The middle column (panels b and e) displays the rebound fraction as a function of

the ambient relative humidity. The last column (panels c and f) displays the apparatus (inlet) relative humidity versus the ambient relative humidity (cf. Table S6).

Figure S5. Rebound fractions measured during (a) IOP1 and (b) IOP2 compared to the background-average reference curve (black lines) and its upper and lower bounds (red lines) (cf. Section S5 of the Supplement). Results are shown for particles having a mobility diameter of 190 nm. The RH values correspond to those inside the impactor.

Figure S6. Rebound curves for a variety of test materials including chamber PM, Amazonia PM measured during 2013, and particles of sucrose, citric acid, and ammonium sulfate. (a) Rebound fractions for < 50% RH. (b) Rebound fractions for > 50% RH. The shaded regions show the full range of rebound fractions measured during IOP1 and IOP2. The background-average values are also plotted for reference.

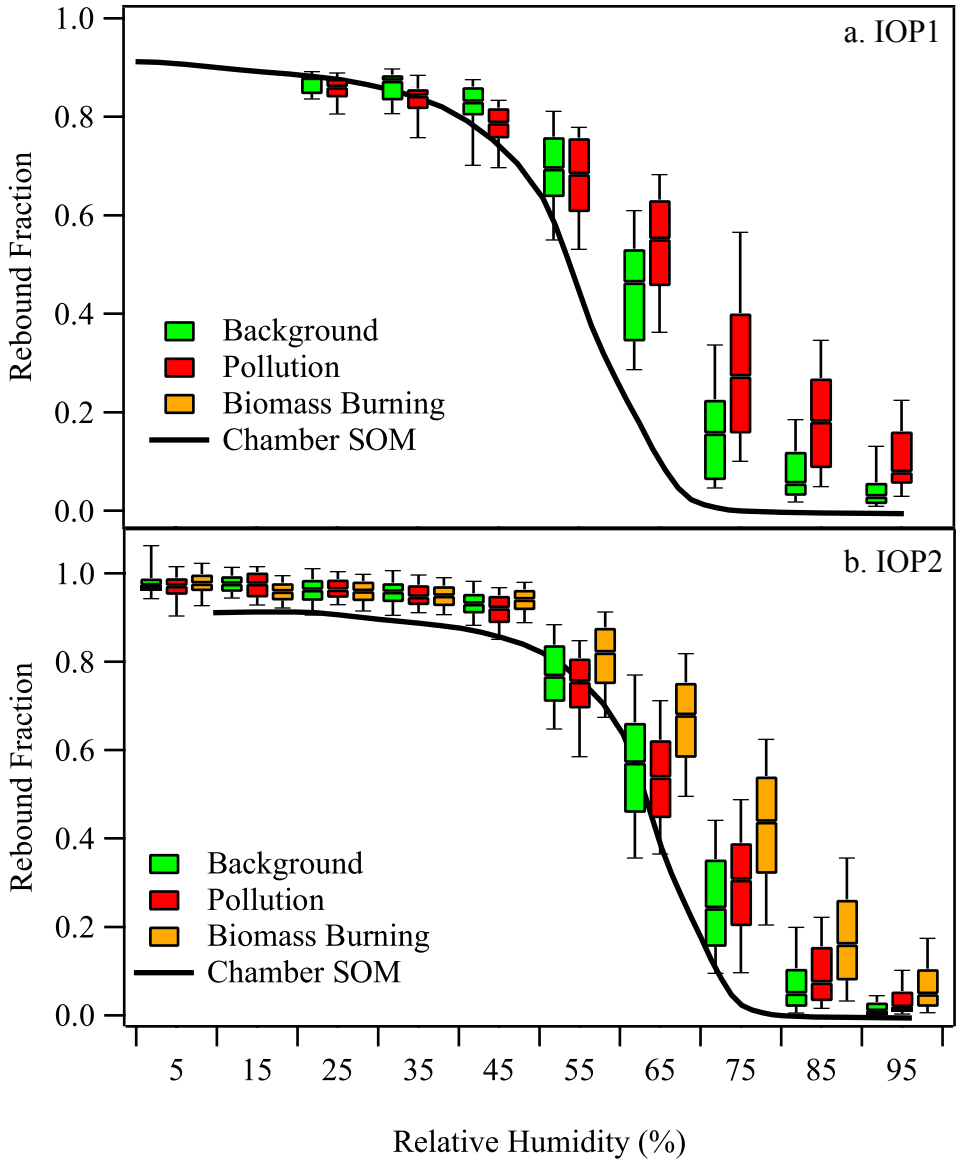
a. IOP1
b. IOP2
Rebound Fraction
1.0
0.8
0.6
0.4
0.2
0.0
Background
Pollution
Biomass Burning
Chamber SOM
5
15
25
35
45
55
65
75
85
95
Relative Humidity (%)

Figure S1

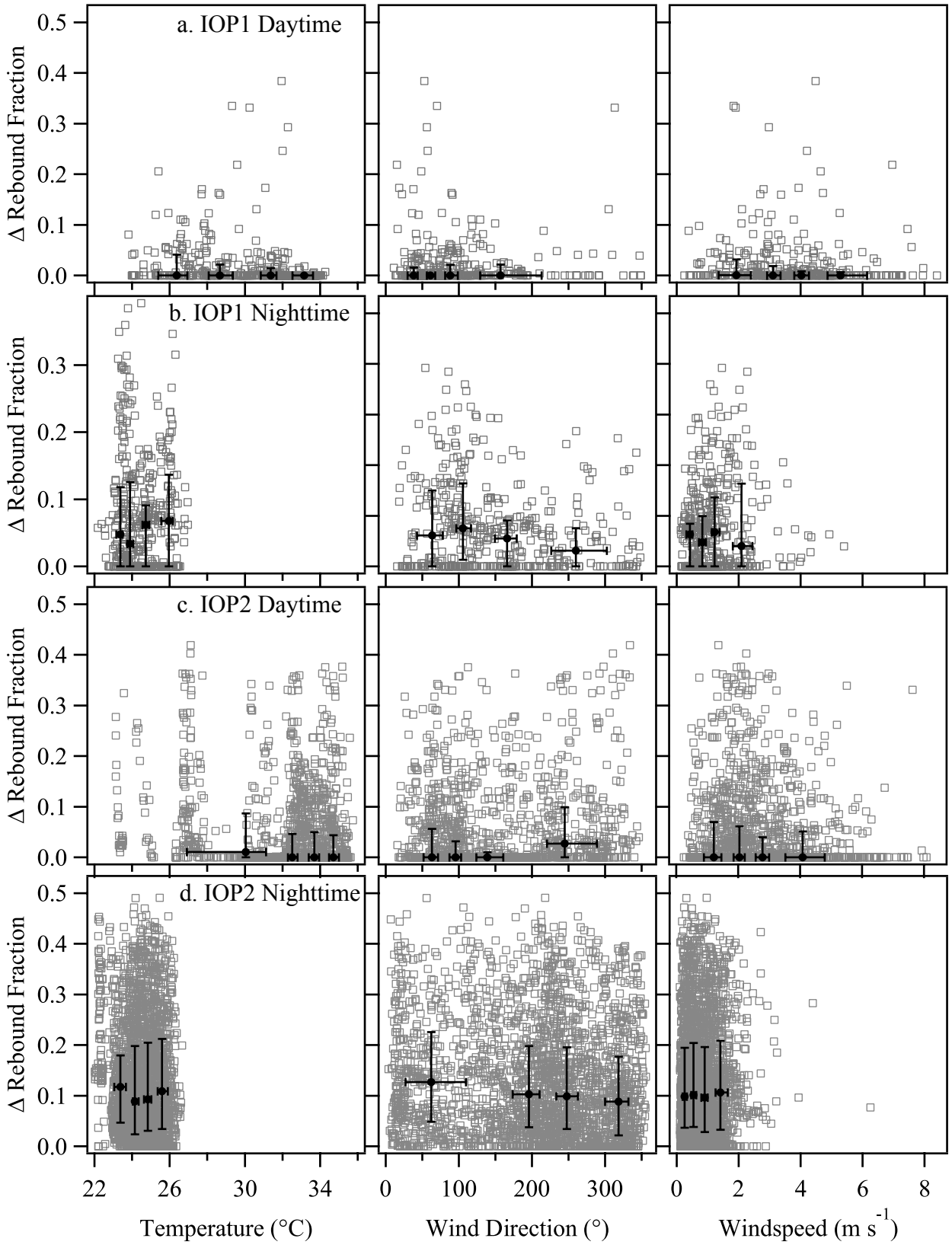
a. IOP1 Daytime
b. IOP1 Nighttime
c. IOP2 Daytime
d. IOP2 Nighttime
Δ Rebound Fraction
0.0
0.1
0.2
0.3
0.4
0.5
22
26
30
34
0
100
200
300
0
2
4
6
8
Temperature (°C)
Wind Direction (°)
Windspeed (m s-1)

Figure S2

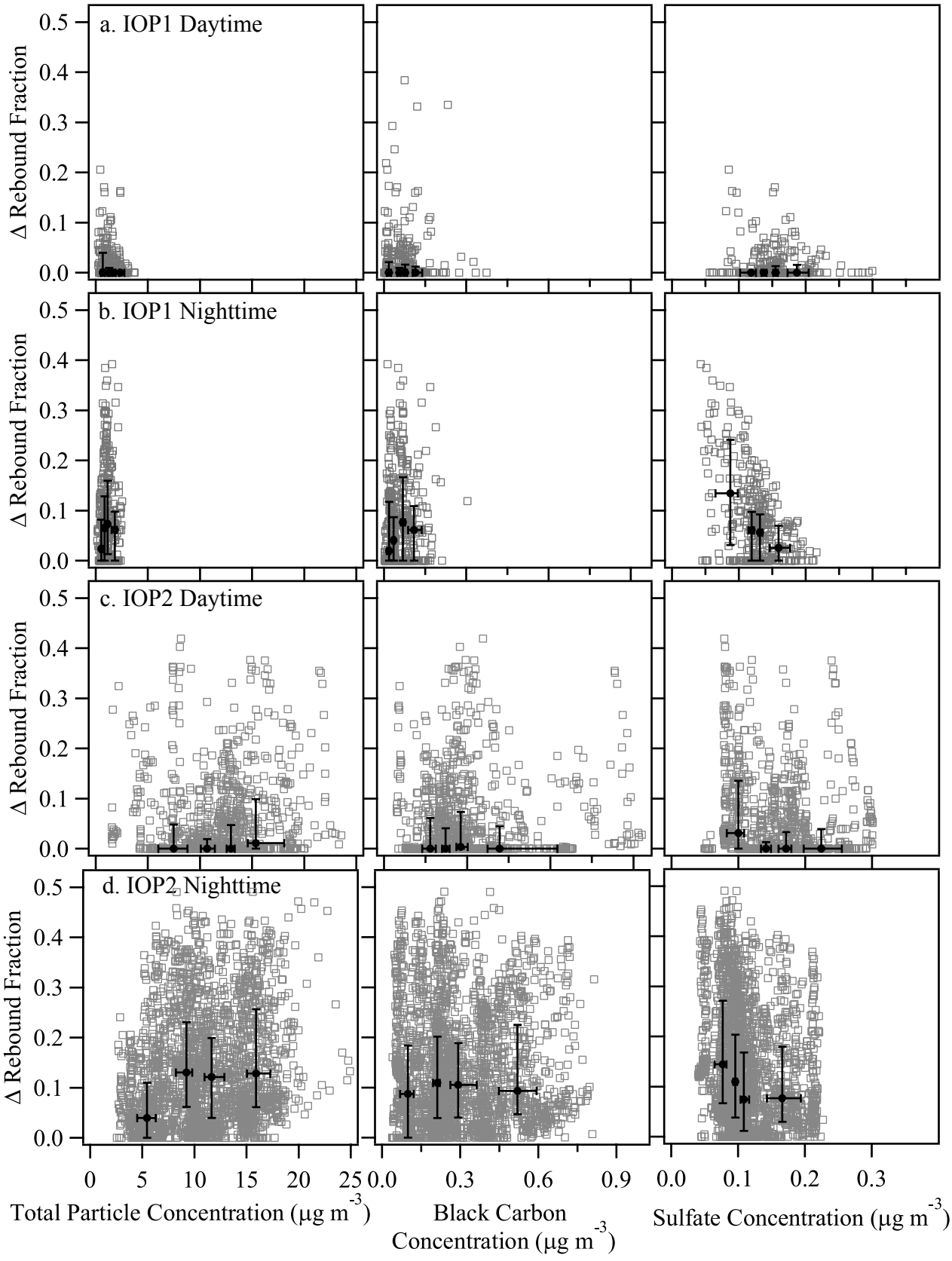
a. IOP1 Daytime
b. IOP1 Nighttime
c. IOP2 Daytime
d. IOP2 Nighttime
Δ Rebound Fraction
0.0
0.1
0.2
0.3
0.4
0.5
0
5
10
15
20
25
0.0
0.3
0.6
0.9
0.0
0.1
0.2
0.3
Total Particle Concentration (μg m-3)
Black Carbon Concentration (μg m-3)
Sulfate Concentration (μg m-3)

Figure S3

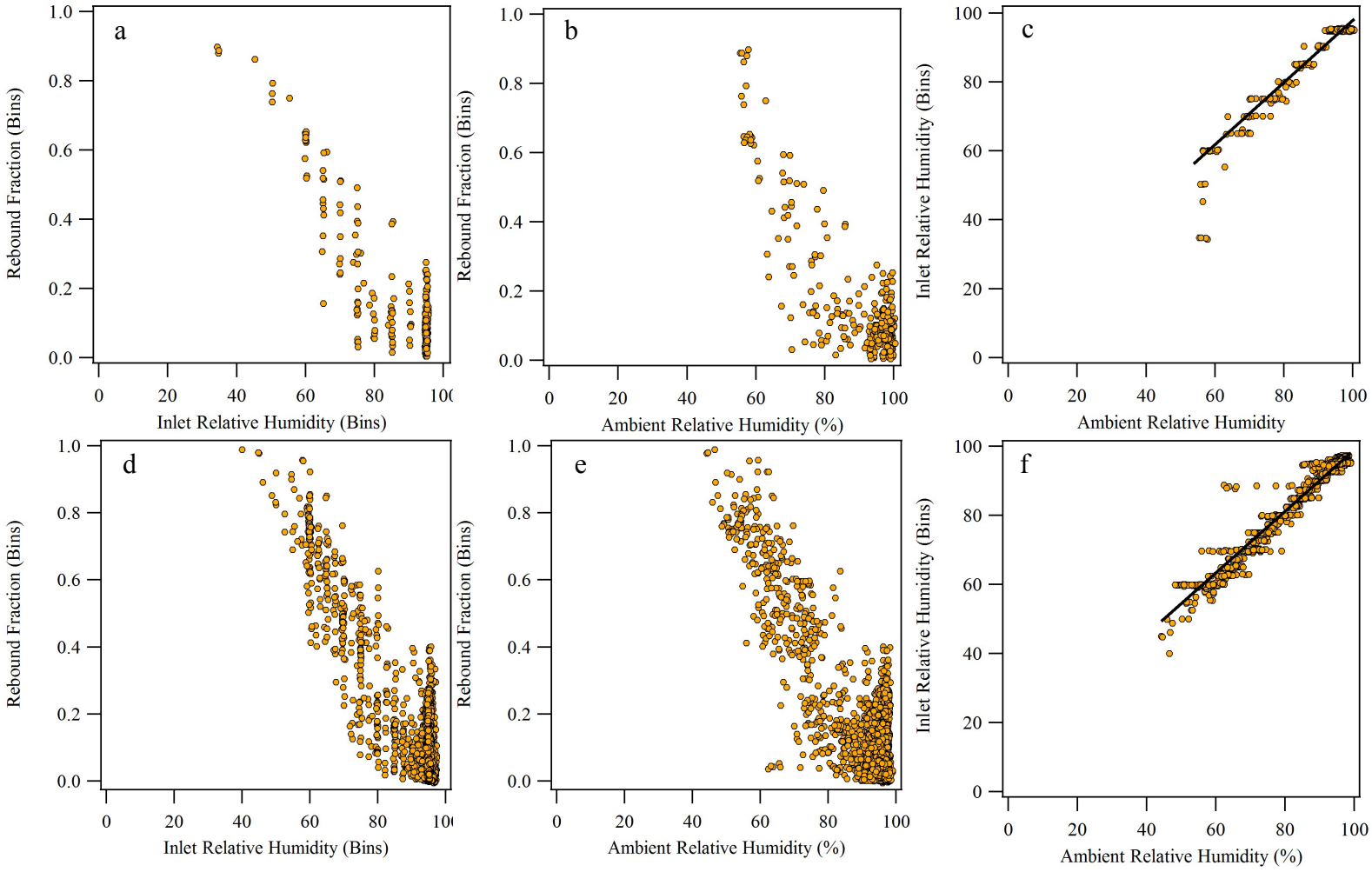
a
b
c
d
e
f
Rebound Fraction (Bins)
Inlet Relative Humidity (Bins)
Ambient Relative Humidity (%)
Inlet Relative Humidity (Bins)
Ambient Relative Humidity
Ambient Relative Humidity (%)

Figure S4

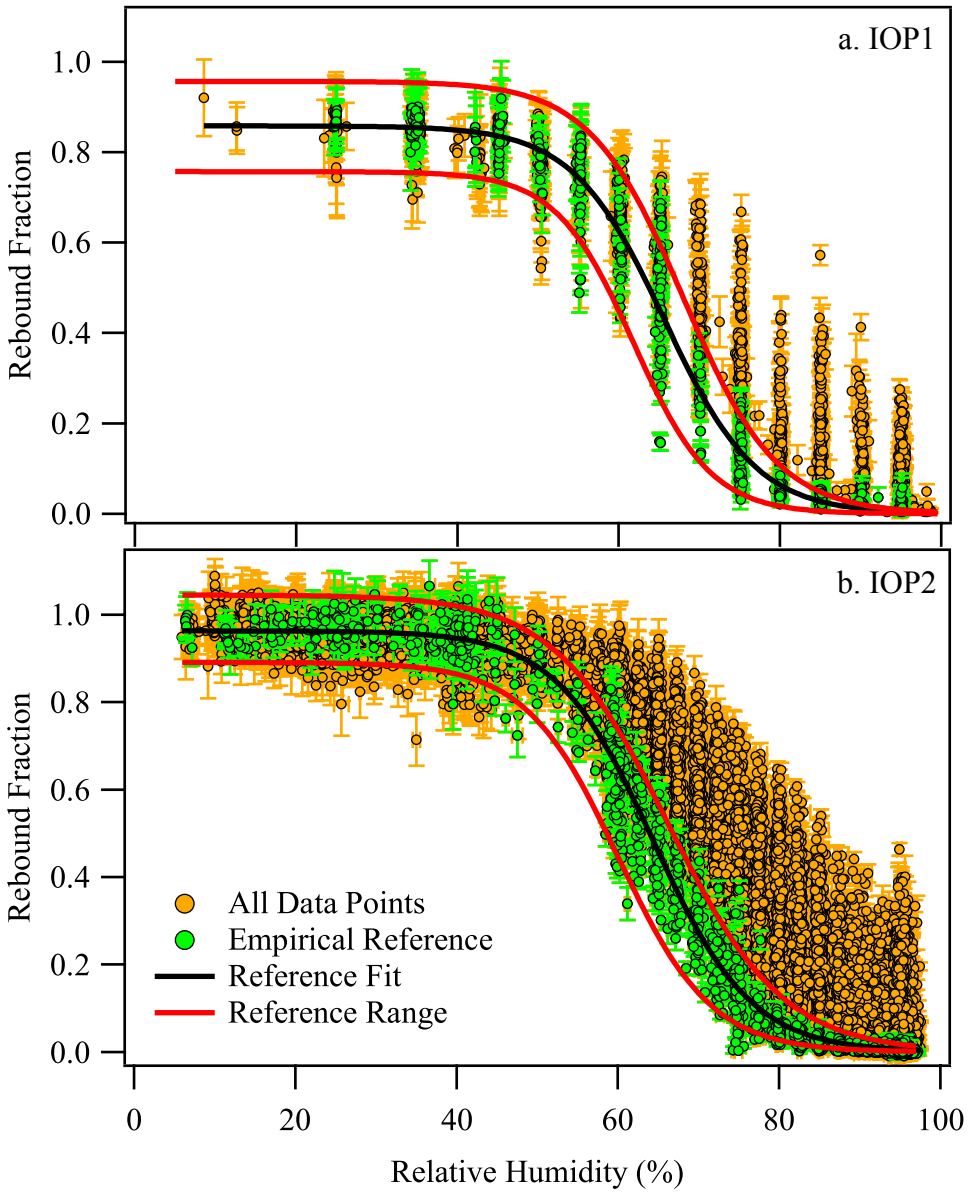
a. IOP1
b. IOP2
Rebound Fraction
Rebound Fraction
1.0
0.8
0.6
0.4
0.2
0.0
All Data Points
Empirical Reference
Reference Fit
Reference Range
0
20
40
60
80
100
Relative Humidity (%)

Figure S5

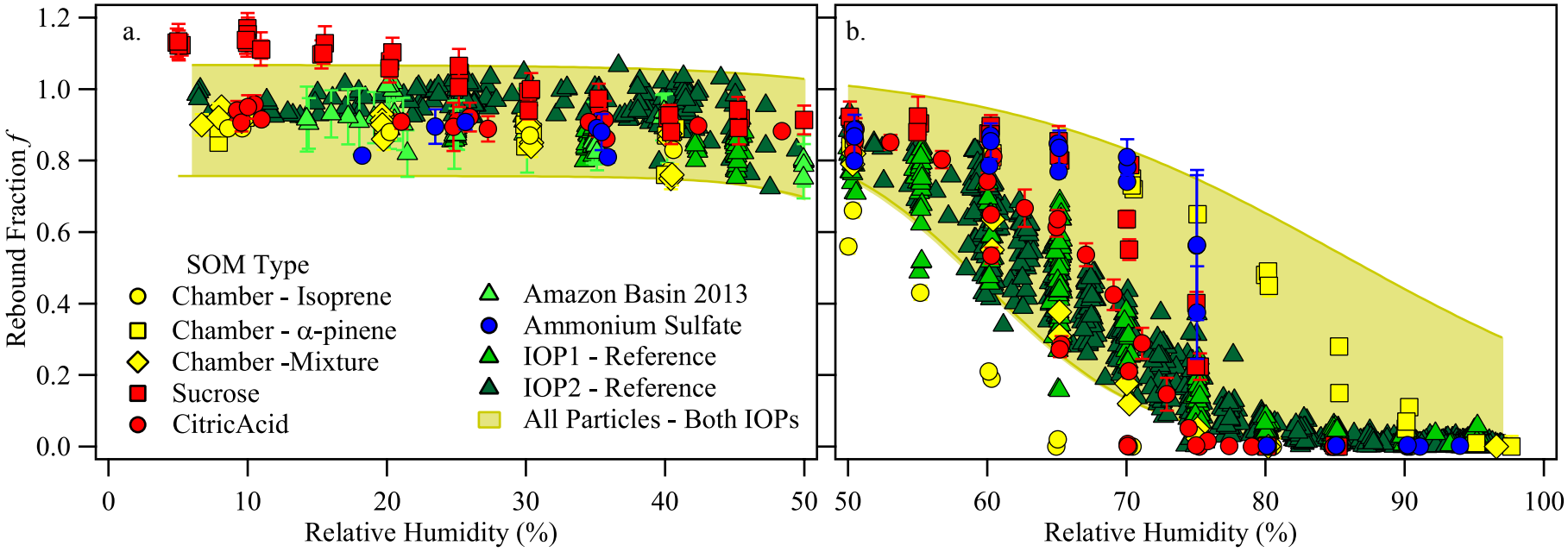
a.
b.
Rebound Fraction f
1.2
1.0
0.8
0.6
0.4
0.2
0.0
0
10
20
30
40
50
60
70
80
90
100
Relative Humidity (%)
Relative Humidity (%)
SOM Type
Chamber - Isoprene
Chamber - α-pinene
Chamber -Mixture
Sucrose
CitricAcid
Amazon Basin 2013
Ammonium Sulfate
IOP1 - Reference
IOP2 - Reference
All Particles - Both IOPs

Figure S6